Sub-radian-accuracy gravitational waves from coalescing binary neutron stars II: Systematic study on the equation of state, binary mass, and mass ratio

Kenta Kiuchi,[1,2] Kawaguchi Kyohei,[3,2,1] Koutarou Kyutoku,[4,5,6,7] Yuichiro Sekiguchi,[8,2] and Masaru Shibata[1,2]

[1] *Max Planck Institute for Gravitational Physics (Albert Einstein Institute), Am Mühlenberg, Potsdam-Golm, 14476, Germany*
[2] *Center for Gravitational Physics, Yukawa Institute for Theoretical Physics, Kyoto University, Kyoto, 606-8502, Japan*
[3] *Institute for Cosmic Ray Research, The University of Tokyo, 5-1-5, Kashiwanoha, Kashiwa, Chiba, 277-8582, Japan*
[4] *Department of Physics, Kyoto University, Kyoto 606-8502, Japan*
[5] *Center for Gravitational Physics, Yukawa Institute for Theoretical Physics, Kyoto University, Kyoto 606-8502, Japan*
[6] *Theory Center, Institute of Particle and Nuclear Studies, KEK, Tsukuba 305-0801, Japan*
[7] *Interdisciplinary Theoretical and Mathematical Sciences Program (iTHEMS), RIKEN, Wako, Saitama 351-0198, Japan*
[8] *Department of Physics, Toho University, Funabashi, Chiba, 274-8510, Japan*

(Dated: July 10, 2019)

We report results of numerical relativity simulations of binary neutron star mergers. We perform simulations for *new* 26 non-spinning binary models with 6 grid resolutions using an adaptive mesh refinement numerical relativity code `SACRA-MPI`. The finest grid spacing is ≈ 64 m. First, we derive long-term high-precision inspiral gravitational waveforms for calibrating the SACRA gravitational waveform template. We find that the accumulated gravitational-wave phase error due to the finite grid resolution is less than 0.5 radian during more than 200 radian phase evolution irrespective of the models. We also find that the gravitational-wave phase error for a model with a tabulated equation of state is comparable to that for a piece-wise polytropic equation of state. Then we calibrate the proposed universal relations between the post-merger gravitational wave signal and tidal deformability/neutron star radius in the literature. We find that they suffer from systematics and many relations proposed as universal are not very universal. We also propose improved fitting formulae. Finally, we validate the SACRA gravitational waveform template which will be used to extract tidal deformability from gravitational wave observation and find that accuracy of our waveform modeling is $\lesssim 0.1$ radian in the gravitational-wave phase and $\lesssim 20\%$ in the gravitational-wave amplitude up to the gravitational-wave frequency 1000 Hz.

PACS numbers: 04.25.D-, 04.30.-w, 04.40.Dg

I. INTRODUCTION

On August 17, 2017, advanced LIGO and advanced Virgo detected gravitational waves from a binary neutron star (BNS) merger, GW170817, for the first time [1]. In this event, not only gravitational waves but also the electromagnetic signals in the gamma-ray [2–4], ultraviolet-optical-infrared [5–20], X-ray [21–23], and radio bands [24–29] were detected. This monumental event GW170817, GRB170817A, and AT2017gfo heralded the opening of the multi-messenger astrophysics. Furthermore, advanced LIGO and advanced Virgo have started a new observation run, O3, from April 2019 and three candidates of a BNS merger as of July 1, 2019, have been detected [30].

One noteworthy finding in GW170817 is that tidal deformability of the neutron star (NS) was constrained for the first time. Due to a tidal field generated by a companion, NSs in a binary system could be deformed significantly in the late inspiral stage [31]. The response to the tidal field, the tidal deformability, is imprinted as a phase shift in gravitational waves and its measurement gives a constraint on the equation of state (EOS) of NSs because the tidal deformability depends on EOSs. GW170817 constrained the binary tidal deformability in the range of $100 \lesssim \tilde{\Lambda} \lesssim 800$ with the binary total mass of $2.73^{+0.04}_{-0.01} M_\odot$ [1, 32–34] where the precise value depends on the analysis methods.

To extract information of the tidal deformability from observed gravitational wave data, a high precision gravitational waveform template plays an essential role. In particular, numerical relativity simulations are the unique tool to derive high-precision gravitational waveforms in the late inspiral stage. During this stage, the gravitational-wave phase shift due to the tidal deformation becomes prominent and any analytic techniques break down. Dietrich and his collaborators constructed a gravitational wave template for the inspiral stage based on the numerical relativity simulations in a series of papers [35–40] and their template was used in gravitational wave data analysis by LIGO Scientific Collaborations to infer the tidal deformability of GW170817 [32]. However, the residual phase error caused mainly by the finite grid resolution in their simulations is $\approx$ 0.5–2.3 radian [40] and the grid resolution in their simulations is lower than that in our previous simulations [41, 42]. The phase error of $O(1)$ radian could be an obstacle to construct a high-quality inspiral gravitational waveform template (see also Refs. [43, 44]).

In Ref. [41], we tackled this problem by using our numerical relativity code `SACRA-MPI` and performed long-term simulations with the highest grid resolution to date

(see also Refs. [45–48] for our effort in the early stage of this project). In our numerical results, the gravitational-wave phase error caused by the finite grid resolution is less than 0.5 radian for 31–32 inspiral gravitational wave cycles. On the basis of these high-precision gravitational waveforms, Ref. [42] presented a waveform template, the SACRA gravitational waveform template, of BNS mergers. Specifically, we multiply the 2.5 Post-Newtonian (PN) order tidal-part phase derived in Ref. [49] by a correction term composed of the PN parameter and the binary tidal deformability. Then, we calibrated it so as to reproduce the high-precision gravitational waveforms derived in Ref. [41]. We also calibrated a correction term in the 1 PN order formula for the tidal-part amplitude derived in Refs. [49, 50].

In Refs. [41, 42], we performed simulations of a limited class of BNS models, i.e., two equal-mass models and two unequal-mass models. Thus, the applicable range of the SACRA gravitational waveform template has not quantified precisely yet. In this paper, we derive a number of gravitational waveforms from BNS mergers by performing numerical-relativity simulations in a wider parameter space for EOSs, binary total mass, and mass ratio than that in the previous papers [41, 42]. In each binary parameter, we perform an in-depth resolution study to assess the accuracy of our waveforms. On the basis of new derived high-precision gravitational waveforms, we validate the SACRA gravitational waveform template.

In addition, we analyze post-merger gravitational wave signals derived in the BNS merger simulations. The post-merger signal in GW170817 has not been detected yet [51], but a post-merger signal could be detected in the near future for the nearby events or with the third generation detectors such as Einstein Telescope or Cosmic Explorer [52, 53]. The signal could bring us complementary information of the EOS to that imprinted in the late inspiral signal. To extract such information, we should explore a heuristic relation between post-merger signals and the tidal deformability/NS radius in numerical relativity simulations. In the previous papers, such an attempt has been made [54–60]. However, systematics contained in these relations are unclear because of the lack of resolution study, approximate treatment of relativistic gravity, and the narrow range of the BNS parameter space. In this paper, we assess to what extent the proposed universal relations between the post-merger gravitational wave signal and tidal deformability/NS radius [54–60] hold.

To stimulate an independent attempt by other researchers for constructing a gravitational waveform template based on the numerical relativity simulations and/or to stimulate a comparison to numerical relativity simulations done by other groups, we release our simulation data on the web. Our numerical-relativity simulation data is available at SACRA Gravitational Waveform Data Bank.

This paper is organized as follows. Section II describes our method, grid setup, and initial condition of the simulations. Section III is devoted to describing SACRA Gravitational Waveform Data Bank, the estimation of the phase error in gravitational waves, and the assessment of the universal relations of the post-merger signals. Section IV presents validation of the SACRA gravitational waveform template. We summarize this paper in Sec. V.

II. METHOD, GRID SETUP, AND INITIAL MODELS

A. Method and grid setup

We use our numerical relativity code, `SACRA-MPI` [41, 61], to simulate a long-term inspiral stage of BNS up to merger. `SACRA-MPI` implements the Baumgarte-Shapiro-Shibata-Nakamura-puncture formulation [62–65], *locally* incorporating a Z4c-type constraint propagation prescription [66], to solve Einstein's equation. We discretize Einstein's equation with the 4th-order accuracy in both the space and time. We also apply the lop-sided finite difference scheme for the advection term [67].

In `SACRA-MPI`, the general relativistic hydrodynamics is formulated in a conservative form and we implement a high-resolution shock capturing scheme proposed by Kurganov and Tadmor [68] together with the 3rd-order accurate cell reconstruction [69].

`SACRA-MPI` implements the Berger-Oliger type adaptive mesh refinement (AMR) algorithm [70] to enlarge a simulation domain to a local wave zone of gravitational waves while guaranteeing a high spatial grid resolution around NSs. A simulation domain consists of two sets of the 4 Cartesian AMR domains which follow orbital motion of each NS and the 6 Cartesian AMR domains whose center is fixed to the coordinate origin throughout all the simulations. `SACRA-MPI` assumes that the grid spacing of a coarser refinement level is twice as large as that of its finer refinement level. Thus, the grid spacing of a refinement level l is given by $\Delta x_l = L/(2^l N)$ with $l = 0, 1, \cdots 9$. L and N denote the distance and the number of grid points from the coordinate origin to the outer boundary along each coordinates axis, respectively. Thus, each AMR domain possesses the grid point $(2N+1, 2N+1, N+1)$ in the x, y, and z directions where we assumed the orbital plane symmetry.

In this work, we performed simulations with $N = 182, 150, 130, 110, 102$, and 90 for all the models to check the convergence of gravitational waveforms with respect to the grid resolution. The values of L and Δx_9 are summarized in Table I.

B. model

Table I shows the list of the models as well as the grid setup for the simulations.

1. Equation of state

Following the previous papers [41, 42], we employ a parameterized piece-wise polytropic EOS to describe the NS matter [71]. Specifically, we assume that the pressure and internal energy consist of two segments with respect to the rest-mass density:

$$P_{\rm cold}(\rho) = \kappa_i \rho^{\Gamma_i},$$
$$\epsilon_{\rm cold}(\rho) = \frac{\kappa_i}{\Gamma_i - 1}\rho^{\Gamma_i - 1} + \Delta\epsilon_i \ (\rho_i \le \rho < \rho_{i+1}),$$

with $i = 0, 1$, $\rho_0 = 0$ g cm^{-3}, and $\rho_2 = \infty$. ρ_1 is the rest-mass density which divides the pressure and internal energy into the two segments. Given the adiabatic indices Γ_0, Γ_1 and a polytropic constant κ_0, another polytropic constant κ_1 is calculated from the continuity of the pressure at $\rho = \rho_1$ by $\kappa_0\rho_1^{\Gamma_0} = \kappa_1\rho_1^{\Gamma_1}$. $\Delta\epsilon_1$ is also calculated from the continuity of the internal energy at $\rho = \rho_1$ by $\kappa_0\rho_1^{\Gamma_0-1}/(\Gamma_0 - 1) = \kappa_1\rho_1^{\Gamma_1-1}/(\Gamma_1 - 1) + \Delta\epsilon_1$. Note that $\Delta\epsilon_0 = 0$. Following Ref. [71], we fix $\Gamma_0 = 1.3562395$, $\Gamma_1 = 3$, and $\kappa_0 = 3.594 \times 10^{13}$ in cgs units. By varying the remaining parameter ρ_1 for a wide range as shown in Table II, we can derive plausible NS models with a variety of the radius and tidal deformability for a given mass (see Table III).

In addition to the piece-wise polytropic EOS, we employ one tabulated EOS, SFHo [72], with the assumption of the neutrinoless low-temperature β-equilibrium condition. Then, the original tabulated EOS is reduced to a one dimensional SFHo (tabulated) EOS, i.e., $P_{\rm cold}(\rho)$ and $\epsilon_{\rm cold}(\rho)$ (see also Table III for the NS radius and tidal deformability).

During simulations, we employ a hybrid EOS to capture the shock heating effect. Specifically, the pressure consists of the cold and thermal parts:

$$P = P_{\rm cold}(\rho) + (\Gamma_{\rm th} - 1)\rho(\epsilon - \epsilon_{\rm cold}(\rho)), \qquad (2.1)$$

where we assumed that the thermal part could be described by the Γ-law EOS with the index $\Gamma_{\rm th}$. Following Refs. [41, 42], we fix $\Gamma_{\rm th} = 1.8$.

2. Model

In this paper, we consider 6 irrotational binary models assuming that NSs have no spin before merger. We fix the chirp mass, $\mathcal{M}_c$, and symmetric mass ratio, η, to be $(\mathcal{M}_c, \eta) = (1.1752M_\odot, 0.2500)$, $(1.1752M_\odot, 0.2485)$, $(1.1752M_\odot, 0.2455)$, $(1.1752M_\odot, 0.2450)$, $(1.0882M_\odot, 0.2470)$, and $(1.0882M_\odot, 0.2440)$. With this setting, gravitational masses of a less massive and massive component for the infinite orbital separation is $(m_1, m_2) = (1.35M_\odot, 1.35M_\odot)$, $(1.25M_\odot, 1.46M_\odot)$, $(1.18M_\odot, 1.55M_\odot)$, $(1.17M_\odot, 1.56M_\odot)$, $(1.12M_\odot, 1.40M_\odot)$, and $(1.07M_\odot, 1.46M_\odot)$ (see Table I). For the SFHo (tabulated) EOS, we only consider the equal-mass binary model with $m_1 = 1.35M_\odot$ and $m_2 = 1.35M_\odot$.

Table I also shows the binary tidal deformability for all the binary models:

$$\tilde{\Lambda} = \frac{8}{13}\Big[(1 + 7\eta - 31\eta^2)(\Lambda_1 + \Lambda_2) - \sqrt{1 - 4\eta}(1 + 9\eta - 11\eta^2)(\Lambda_1 - \Lambda_2)\Big], \qquad (2.2)$$

where $\Lambda_1(\Lambda_2)$ is the tidal deformability of the less massive (massive) component. The value of the tidal deformability in this paper covers a wide range of $\approx$ 300–1800.

Figure 1 plots the BNS models simulated by our group. For the SFHo (tabulated) EOS case, an interpolation of the thermodynamic variables is necessary in the simulations. This could be an error budget for generating high-precision gravitational waveforms. This model is used to assess the error budget.

We name each model according to the EOS, the mass of the less massive component, and that of the massive component. For example, 15H125-146 means the model with 15H EOS, $m_1 = 1.25M_\odot$, and $m_2 = 1.46M_\odot$. We set the initial orbital angular velocity to be $Gm_0\Omega_0/c^3 = 0.015$–0.0155. With this, the BNSs experience about 15–16 orbits before the onset of merger for all the models.

To generate a high-precision inspiral waveform from a BNS merger by a numerical relativity simulation, initial data with low orbital eccentricity is necessary because the orbital motion of a BNS just before merger is circularized due to the gravitational-wave emission. We numerically obtain quasi equilibrium sequences of the BNSs by a spectral-method library, LORENE [73, 74]. Then, we perform an orbital eccentricity reduction by using the prescription in Ref. [75]. With this method, we confirm that the initial orbital eccentricity is typically reduced to $\approx 10^{-3}$ which is low enough to generate a high-precision inspiral waveform (see also Appendix in Refs. [41, 42]).

C. Gravitational wave extraction

We calculate a complex Weyl scalar Ψ_4 from simulation data to derive gravitational waveforms [61]. Given an extraction radius r_0, the Weyl scalar Ψ_4 is decomposed into (l, m) mode with the spin-weighted spherical harmonics by

$$\Psi_4(t_{\rm ret}, r_0, \theta, \phi) = \sum_{l,m} \Psi_4^{l,m}(t_{\rm ret}, r_0)\,{}_{-2}Y_{lm}(\theta, \phi), \qquad (2.3)$$

where $t_{\rm ret}$ is a retarded time. It is defined by

$$t_{\rm ret} \equiv t - \left[D + 2m_0 \ln\left(\frac{D}{2m_0} - 1\right)\right], \qquad (2.4)$$

where $D = \sqrt{A/4\pi}$ and A is a proper area of the extraction sphere. We apply Nakano's method [76] to extrapo-

late $\Psi_4^{l,m}$ to infinity by

$$D\Psi_4^{l,m,\infty}(t_{\rm ret})|_{D\to\infty} = C(r_0)\Big[D\Psi_4^{l,m}(t_{\rm ret}, r_0) - \frac{(l-1)(l+2)}{2}\int^{t_{\rm ret}} \Psi_4^{l,m}(t', r_0)dt'\Big], \quad (2.5)$$

where $C(r_0)$ is a function of r_0. Following Ref. [41], we choose $D = r_0[1 + m_0/(2r_0)]^2$ and $C(r_0) = 1 - 2m_0/D$ because our coordinate is similar to isotropic coordinates of non-rotating black holes.

Gravitational waves of each mode is calculated by integrating $\Psi_4^{l,m,\infty}$ twice in time:

$$h^{l,m,\infty}(t_{\rm ret}) = h_+^{l,m,\infty}(t_{\rm ret}) - ih_\times^{l,m,\infty}(t_{\rm ret}) = -\int^{t_{\rm ret}} dt' \int^{t'} \Psi_4^{l,m,\infty}(t'')dt''. \quad (2.6)$$

For the time integration, we employ the fixed frequency method [77] by

$$h^{l,m,\infty}(t_{\rm ret}) = \int df' \frac{\tilde{\Psi}_4^{l,m,\infty}(f')}{(2\pi \max[f', f_{\rm cut}])^2} \exp(2\pi i f' t_{\rm ret}), \quad (2.7)$$

where $\tilde{\Psi}_4^{l,m,\infty}(f)$ is the Fourier component of $\Psi_4^{l,m,\infty}(t)$ and $f_{\rm cut}$ is set to be $0.8m\Omega_0/(2\pi)$.

To check the convergence with respect to the extraction radius r_0, we repeat this analysis for $r_0 = 244\,m_0$, $199\,m_0$, and $155\,m_0$ for $\mathcal{M}_c = 1.1752M_\odot$ and $r_0 = 262\,m_0$, $213\,m_0$, and $156\,m_0$ for $\mathcal{M}_c = 1.0882M_\odot$ (see Table I).

In general, gravitational waves are decomposed into the amplitude and phase by

$$h^{l,m,\infty}(t_{\rm ret}) = A^{l,m,\infty}(t_{\rm ret})e^{-i\Phi(t_{\rm ret})}, \quad (2.8)$$

and instantaneous gravitational-wave frequency, $f_{\rm GW}$, is defined by $d\Phi/dt$. With Eq. (2.8), the frequency of the $(l, m) = (2, 2)$ mode is calculated by

$$f_{\rm GW} = \frac{1}{2\pi}{\rm Im}\left(\frac{h^{*2,2,\infty}\dot{h}^{2,2,\infty}}{|h^{2,2,\infty}|^2}\right) \quad (2.9)$$

where $h^{*2,2,\infty}$ is the complex conjugate of $h^{2,2,\infty}$.

We also calculate the energy and angular momentum fluxes due to gravitational-wave emission by [78]

$$\frac{dE_{\rm GW}^{l,m}}{dt} = \lim_{r\to\infty}\frac{r^2}{16\pi}\left|\int^t \Psi_4^{l,m,\infty}(t')dt'\right|^2,$$
$$\frac{dJ_{\rm GW}^{l,m}}{dt} = -\lim_{r\to\infty}\frac{r^2}{16\pi}{\rm Im}\Big[m\left(\int^t \Psi_4^{l,m,\infty}(t')dt'\right)^* \times \int^t dt' \int^{t'} dt''\Psi_4^{l,m,\infty}(t'')\Big]. \quad (2.10)$$

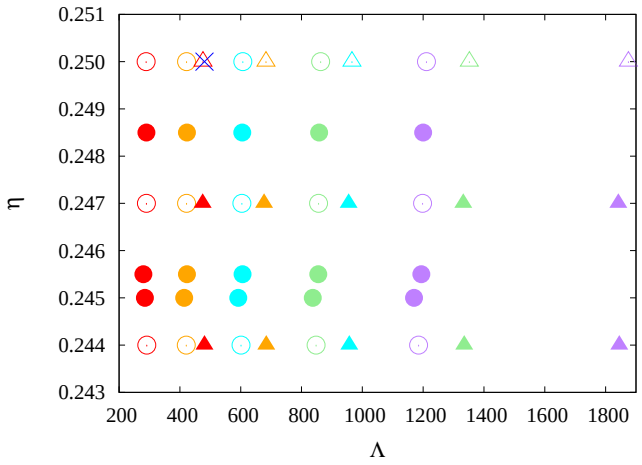

FIG. 1. Symmetric mass ratio, η, and binary tidal deformability, $\tilde{\Lambda}$, simulated by our group. The circle and triangle symbols denote BNS models with $\mathcal{M}_c = 1.1752M_\odot$ and with $\mathcal{M}_c = 1.0882M_\odot$, respectively. The open symbols denote the models reported in Refs. [41, 42]. The filled symbols are the models newly employed in this study. The purple, green, cyan, orange, and red colors are for the models with EOS 15H, 125H, H, HB, and B, respectively. The blue cross symbol is for SFHo135-135.

Thus, the energy and angular momentum carried by gravitational waves are calculated by

$$E_{\rm GW}^{l,m} = \int \frac{dE_{\rm GW}^{l,m}}{dt}dt,$$
$$J_{\rm GW}^{l,m} = \int \frac{dJ_{\rm GW}^{l,m}}{dt}dt. \quad (2.11)$$

III. RESULTS

A. Gravitational waveform data bank

We have simulated 46 binary models with 6 grid resolutions. Our waveform data is publicly available on the web:

SACRA Gravitational Waveform Data Bank [79].

On the website, we tabulate the waveform data according to the model name, dimensionless initial orbital angular velocity, and grid resolution. For example, 15H_135_135_00155_182 indicates that the employed EOS is 15H, $m_1 = 1.35M_\odot$, $m_2 = 1.35M_\odot$, $Gm_0\Omega_0/c^3 = 0.0155$, and $N = 182$ (see also Table I). A user can download the data for $\Psi_4^{2,2}(t_{\rm ret}, r_0)$ extracted at several values of r_0 and $h_{+,\times}^{2,2,\infty}(t_{\rm ret})$ from the link on the model name.

TABLE I. List of the models. Model name is given in the 1st column. The 2nd and 3rd columns show gravitational mass of less massive NS, m_1, and massive NS, m_2, respectively. The 4th column shows EOS. Dimensionless initial orbital angular velocity, Ω_0, with the total gravitational mass of the binaries, $m_0 = m_1 + m_2$, is given in the 5th column. The 6th, 7th, and 8th columns show chirp mass, $\mathcal{M}_c = (m_1 m_2)^{3/5}(m_1 + m_2)^{-1/5}$, symmetric mass ratio, $\eta = m_1 m_2 (m_1 + m_2)^{-2}$, and binary tidal deformability, $\tilde{\Lambda}$, respectively. Location of outer boundary in a computational domain, L, and grid spacing of a finest adaptive mesh refinement level, Δx_9, are given in the 9th and 10th columns, respectively. The grid spacing with $N = 182, 150, 130, 110, 102$, and 90 is shown in the parenthesis in the 10th column. The final column shows the extraction radii of gravitational waves.

Model	m_1 $[M_\odot]$	m_2 $[M_\odot]$	EOS	$Gm_0\Omega_0/c^3$	$\mathcal{M}_c$	η	$\tilde{\Lambda}$	L [km]	Δx_9 [m]	r_0/m_0
15H125-146	1.25	1.46	15H	0.0155	1.1752	0.2485	1200	7823	(84,102,117,138,149,169)	(244,199,155)
125H125-146	1.25	1.46	125H	0.0155	1.1752	0.2485	858	7323	(78,95,110,129,140,158)	(244,199,155)
H125-146	1.25	1.46	H	0.0155	1.1752	0.2485	605	6824	(73,89,102,121,130,147)	(244,199,155)
HB125-146	1.25	1.46	HB	0.0155	1.1752	0.2485	423	6491	(69,84,97,115,124,140)	(244,199,155)
B125-146	1.25	1.46	B	0.0155	1.1752	0.2485	290	5992	(64,78,90,106,114,129)	(244,199,155)
15H118-155	1.18	1.55	15H	0.0155	1.1752	0.2455	1194	7889	(84,102,118,139,150,170)	(242,198,154)
125H118-155	1.18	1.55	125H	0.0155	1.1752	0.2455	855	7390	(79,96,111,131,141,159)	(242,198,154)
H118-155	1.18	1.55	H	0.0155	1.1752	0.2455	606	6990	(75,91,105,124,133,151)	(242,198,154)
HB118-155	1.18	1.55	HB	0.0155	1.1752	0.2455	423	6491	(69,84,97,115,124,140)	(242,198,154)
B118-155	1.18	1.55	B	0.0155	1.1752	0.2455	292	5992	(64,78,90,106,114,129)	(242,198,154)
15H117-156	1.17	1.56	15H	0.0155	1.1752	0.2450	1170	7889	(84,102,118,139,150,170)	(242,198,154)
125H117-156	1.17	1.56	125H	0.0155	1.1752	0.2450	837	7323	(78,95,110,129,140,158)	(242,198,154)
H117-156	1.17	1.56	H	0.0155	1.1752	0.2450	592	6990	(75,91,105,124,133,151)	(242,198,154)
HB117-156	1.17	1.56	HB	0.0155	1.1752	0.2450	414	6491	(69,84,97,115,124,141)	(242,198,154)
B117-156	1.17	1.56	B	0.0155	1.1752	0.2450	285	6058	(65,79,91,107,115,131)	(242,198,154)
15H112-140	1.12	1.40	15H	0.0150	1.0882	0.2470	1842	7989	(85,104,120,141,152,172)	(262,214,167)
125H112-140	1.12	1.40	125H	0.0150	1.0882	0.2470	1332	7490	(80,97,112,132,143,162)	(262,214,167)
H112-140	1.12	1.40	H	0.0150	1.0882	0.2470	955	6990	(75,91,105,124,133,151)	(262,214,167)
HB112-140	1.12	1.40	HB	0.0150	1.0882	0.2470	677	6491	(69,84,97,115,124,140)	(262,214,167)
B112-140	1.12	1.40	B	0.0150	1.0882	0.2470	475	6092	(65,79,91,108,116,131)	(262,214,167)
15H107-146	1.07	1.46	15H	0.0150	1.0882	0.2440	1845	7989	(85,104,120,141,152,172)	(261,213,166)
125H107-146	1.07	1.46	125H	0.0150	1.0882	0.2440	1335	7490	(80,97,112,132,143,162)	(261,213,166)
H107-146	1.07	1.46	H	0.0150	1.0882	0.2440	957	6990	(75,91,105,124,133,151)	(261,213,166)
HB107-146	1.07	1.46	HB	0.0150	1.0882	0.2440	684	6591	(71,86,99,117,126,142)	(261,213,166)
B107-146	1.07	1.46	B	0.0150	1.0882	0.2440	481	6091	(65,79,91,108,116,131)	(261,213,166)
SFHo135-135	1.35	1.35	SFHo	0.0155	1.1752	0.2500	460	6491	(69,84,97,115,124,140)	(244,200,156)

TABLE II. List of ρ_1 in two piece-wise polytropic EOSs.

EOS	ρ_1[g cm^{-3}]
15H	9.3108×10^{13}
125H	1.0711×10^{14}
H	1.2323×10^{14}
HB	1.4177×10^{14}
B	1.6309×10^{14}

The top panel of Fig. 2 shows the dependence of the gravitational waveforms on the EOSs for the binaries with $m_1 = 1.12M_\odot$, $m_2 = 1.40M_\odot$ and $N = 182$. It shows that the models with the larger values of $\tilde{\Lambda}$ merge earlier than those with the smaller values of $\tilde{\Lambda}$ because the tidal force is the attractive force and the tidal deformation accelerates the orbital shrink. The bottom panel of Fig. 2 shows the dependence of the gravitational waveforms on the symmetric mass ratio for the binaries with 15H125-125, 15H112-140, and 15H107-146 with $N = 182$. It shows that the models with the larger values of η merge earlier than those with the smaller values of η.

The top panel of Fig. 3 shows the dependence of the gravitational waveforms on the grid resolutions for 15H112-140 with $N = 182, 110$, and $N = 90$. Errors in the amplitude and phase caused by the finite grid resolution become prominent for the late inspiral and post-merger stages. This indicates that the gravitational-wave phase shift is also caused by the finite grid resolution. The bottom panel of Fig. 3 plots the phase shift between the models with $m_1 = 1.12M_\odot$, $m_2 = 1.40M_\odot$, and $N = 182$. The phase shift is defined by $\Delta\Phi = \Phi(\mathrm{EOS}) - \Phi(B)$ with EOS = 15H, 125H, H, and HB. The shaded region shows the *numerically induced* phase shift, i.e., phase er-

TABLE III. Equations of state employed, the radius, R_M, and the dimensionless tidal deformability, Λ_M, for spherical NSs with gravitational mass $M = 1.07$, 1.12, 1.17, 1.18, 1.25, 1.35, 1.40, 1.46, 1.55 and $1.56\,M_\odot$. R_M is listed in units of km. For SFHo (tabulated) EOS, the quantities for the spherical star with $M = 1.35\,M_\odot$ are listed. The last column in the upper table is the maximum mass of the spherical NS in units of $M_\odot$.

EOS	$R_{1.07}$	$R_{1.12}$	$R_{1.17}$	$R_{1.18}$	$R_{1.25}$	$R_{1.35}$	$R_{1.40}$	$R_{1.46}$	$R_{1.55}$	$R_{1.56}$	$M_{\rm max}$
15H	13.54	13.58	13.61	13.62	13.65	13.69	13.71	13.72	13.74	13.74	2.53
125H	12.86	12.89	12.91	12.92	12.94	12.97	12.98	12.99	12.98	12.98	2.38
H	12.22	12.23	12.24	12.24	12.26	12.27	12.28	12.18	12.26	12.25	2.25
HB	11.60	11.59	11.60	11.60	11.61	11.61	11.60	11.59	11.55	11.55	2.12
B	10.97	10.97	10.98	10.98	10.98	10.96	10.95	10.92	10.87	10.86	2.00
SFHo	–	–	–	–	–	11.91	–	–	–	–	2.06

EOS	$\Lambda_{1.07}$	$\Lambda_{1.12}$	$\Lambda_{1.17}$	$\Lambda_{1.18}$	$\Lambda_{1.25}$	$\Lambda_{1.35}$	$\Lambda_{1.40}$	$\Lambda_{1.46}$	$\Lambda_{1.55}$	$\Lambda_{1.56}$
15H	4361	3411	2692	2575	1871	1211	975	760	530	509
125H	3196	2490	1963	1875	1351	863	693	535	366	350
H	2329	1812	1415	1354	966	607	484	369	249	238
HB	1695	1304	1013	966	684	422	333	252	165	157
B	1216	933	719	681	477	289	225	168	107	101
SFHo	–	–	–	–	–	460	–	–	–	–

ror, between $N = 182$ and $N = 150$ (red) and between $N = 182$ and $N = 90$ (blue), respectively, for 15H112-140. The phase error is defined by $\Delta\Phi = \Phi(N) - \Phi(182)$ with $N = 150$ and 90. The vertical dashed line denotes the peak time at which the gravitational-wave amplitude becomes maximal for 15H112-140 with $N = 182$. Just after the peak time, gravitational waves become a short-term burst-type waves as shown in the upper panel of Fig. 3, i.e., for 58 ms $\lesssim t_{\rm ret} \lesssim$ 59 ms. These waves cause very rapid increase in the phase during this time interval and consequently the phase shift between the binaries with the different EOSs shows very rapid increase. This feature can be also seen in the phase error and the very rapid increase appears later in the phase shift between $N = 182$ and 150 than that between $N = 182$ and $N = 90$ because the peak time becomes later with improving the grid resolution.

The phase shift up to the peak time among the different EOSs and that among the different grid resolutions are comparable, in particular, for the case with the coarser grid resolution. Therefore unless a thorough convergence study is carried out a capability of numerical relativity inspiral waveforms to measure the tidal deformability is unclear. This is also the case for the the post-merger stage. In particular, the phase shift loosens the convergence as can be seen in the bottom panel of Fig. 3, i.e., the phase error between $N = 182$ and 150 (red shaded region) is higher than that between $N = 182$ and $N = 90$ (blue shaded region). Therefore, the time-domain post-merger gravitational waves are not very reliable. Instead, we will discuss the post-merger signal in terms of the energy and angular momentum carried by gravitational waves and the power spectrum density of gravitational waves. These quantities are calculated by a time integration of the gravitational waveforms and the loss of the convergence in the phase could be irrelevant as discussed in Sec. III D.

B. Estimation of the phase error in gravitational waves

Following Refs. [41, 42], we estimate the gravitational-wave phase error due to the finite grid resolution. The left panel of Fig. 4 plots evolution of the gravitational-wave phase error with different grid resolutions for B107-146. The phase error is defined by $\delta\Phi = \Phi(N) - \Phi(182)$ with $N = 150, 130, 110, 102$, and 90 in this figure. The vertical dashed line denotes the peak time. Although the phase error is accumulated with time, its value at the peak time becomes small as improving the grid resolution. Thus, the gravitational-wave phase error due to the finite grid resolution is reduced as improving the grid resolution.

We estimate a residual phase error by assuming that the gravitational-wave phase at the peak time obeys a following functional form;

$$\Phi_{\rm peak}(N) = \Phi^{\infty}_{\rm peak}(N_{\rm max}) - \Delta\Phi(N_{\rm max}) \left(\frac{N_{\rm max}}{N}\right)^p, \tag{3.1}$$

where $\Phi_{\rm peak}(N)$ is the gravitational-wave phase at the peak time derived from a simulation with the grid number N. $N_{\rm max}$ denotes a reference grid value of N to estimate unknown quantities $\Phi^{\infty}_{\rm peak}(N_{\rm max})$, $\Delta\Phi(N_{\rm max})$, and p. For example, with $N_{\rm max} = 182$, these unknowns are obtained by fitting the simulation results of $N = 150, 130, 110, 102$, and 90 with Eq. (3.1). $\Delta\Phi(N_{\rm max})$ should be recognized as the residual phase error for the simulation with $N = N_{\rm max}$ because $N \to \infty$ means a continuum limit with respect to the grid resolution. Also, p denotes an order of the convergence of the gravitational-wave phase at the peak time.

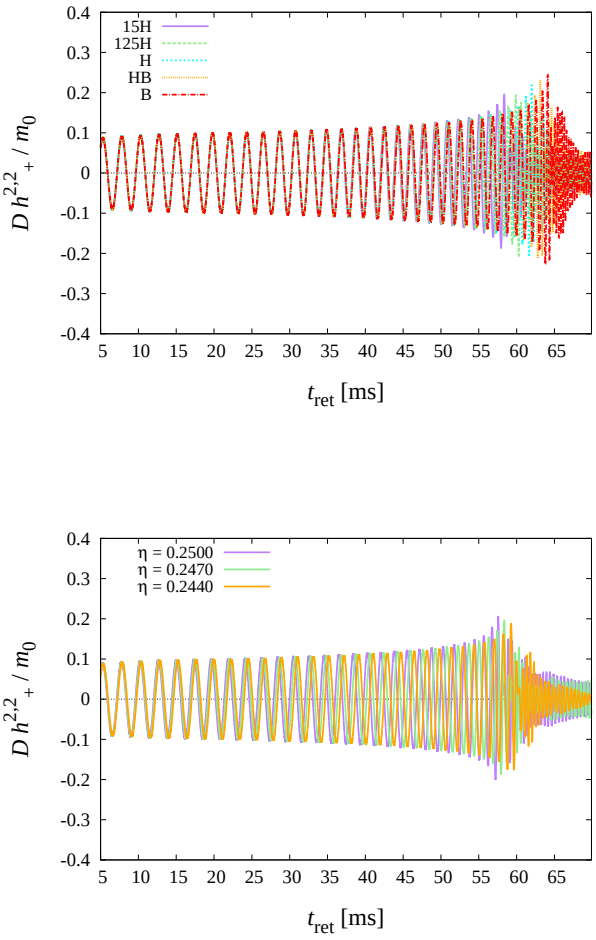

FIG. 2. (Top) h_+ for the $(l,m)=(2,2)$ mode of the gravitational waveforms for the binaries with $m_1 = 1.12M_\odot$ and $m_2 = 1.40M_\odot$. (Bottom) The same as the top panel, but for 15H125-125, 15H112-140, and 15H107-146. In both the panels, the grid resolution is $N = 182$.

The right panel of Fig. 4 plots the gravitational-wave phase error at the peak time as a function of $1/N^p$ with a reference grid number $N_{\rm max}$;

$$\Phi_{\rm peak}(N_{\rm max}) - \Phi_{\rm peak}(N) = \Delta\Phi(N_{\rm max})\left[\left(\frac{N_{\rm max}}{N}\right)^p - 1\right]. \tag{3.2}$$

The values of $\Delta\Phi(N_{\rm max})$ and p are shown in the legend of this figure. It is clear that the order of the convergence p is improved and the residual gravitational-wave phase error is reduced as increasing $N_{\rm max}$. This illustrates that well resolved simulations with at least the grid spacing of ≈ 100 m are necessary to derive gravitational waveforms with sub-radian accuracy.

Table IV summarizes the residual phase error and the order of the convergence of the gravitational-wave phase at the peak time for all the models. We estimate the residual phase error with respect to three reference values of $N_{\rm max}$ as $182, 150$, and 130. In some models, the residual phase error and the order of the convergence show an irregular behavior. That is the residual phase error (the order of the convergence) for $N_{\rm max} = 130$ happens to be smaller (higher) than that for $N_{\rm max} = 150$. Nonetheless, the residual phase error (the order of the convergence) for $N_{\rm max} = 182$ is smaller (higher) than that for $N_{\rm max} = 150$ except for 125H125-146. Thus, we adopt the values for $N_{\rm max} = 182$ as the residual phase error in our waveforms and it is in the range of ≈ 0.1–0.5 radian.

For the SFHo (tabulated) EOS case, we find that the residual phase error still remains within sub-radian. Because SFHo135-135 and HB135-135 have a similar value of $\tilde{\Lambda}$, they are used to estimate the phase error due to the tabulated EOS. For HB135-135, the residual phase error and the order of the convergence are $(\Delta\Phi_{\rm peak}(182), p) = (0.17, 3.6)$, $(\Delta\Phi_{\rm peak}(150), p) = (0.48, 3.2)$, and $(\Delta\Phi_{\rm peak}(130), p) =$

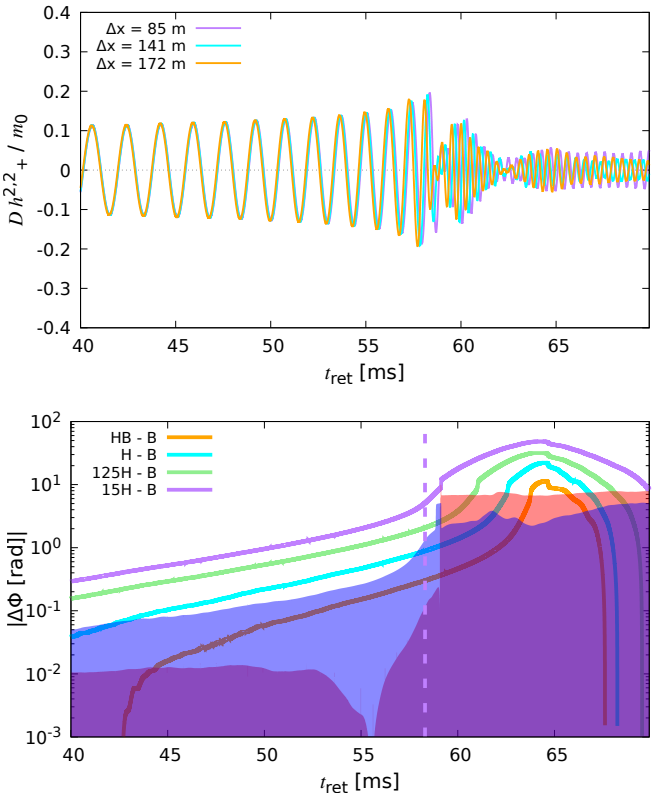

FIG. 3. (Top) The same as Fig. 2, but for 15H112-140 with $N = 182, 110$, and 90. (Bottom) The gravitational-wave phase shift for the binaries with $m_1 = 1.12M_\odot$ and $m_2 = 1.40M_\odot$, and $N = 182$. The shaded region shows the phase shift between $N = 182$ and $N = 150$ (red) and between $N = 182$ and $N = 90$ (blue) for 15H112-140. The overlapping region has purple color. The vertical dashed line denotes the peak time of the gravitational-wave amplitude for 15H112-140 with $N = 182$.

$(2.0, 1.7)$, respectively. For SFHo135-135, the residual phase error and the order of the convergence are $(\Delta\Phi_{\rm peak}(182), p) = (0.43, 2.3)$, $(\Delta\Phi_{\rm peak}(150), p) = (0.76, 2.2)$, and $(\Delta\Phi_{\rm peak}(130), p) = (0.33, 4.2)$, respectively. Thus, the SFHo (tabulated) EOS model has slightly larger residual phase error than the piece-wise polytropic EOS model. This indicates that the interpolation of the thermodynamic quantities could produce a phase error of ≈ 0.2–0.3 radian. Nonetheless, it is encouraging that our waveforms have sub-radian accuracy even for the SFHo (tabulated) EOS case. For more detailed estimate of the error budget due to tabulated EOSs, we need to perform more BNS simulations with tabulated EOSs.

C. Assessment of universality relation

Instantaneous gravitational-wave frequency defined by Eq. (2.9) at some characteristic time in the late inspiral or post-merger stage is reported to be correlated with the tidal deformability or the tidal coupling constant [54, 55, 57, 58]. Characteristic peak frequencies imprinted in the power spectrum density of gravitational waves are reported to be correlated with the tidal coupling constant or NS radius [45, 55, 60, 80]. We assess these proposed universal relations using our waveform data in which a systematic study has been done in a wide range of the binary parameter with a large range of the grid resolution of the simulations. We also explicitly express the relations as a function of the binary tidal deformability.

1. *Peak frequency and binary tidal deformability relation*

Reference [54] reported that the instantaneous gravitational-wave frequency at the peak time $f_{\rm peak}$ has a tight correlation with the binary tidal deformability $\tilde{\Lambda}$ (see also Refs. [55, 57, 58] for the relation with the tidal coupling constant. In Ref. [55], they referred to it as $f_{\rm max}$). Figure 5 plots the dependence of $f_{\rm peak}$ on the grid resolution where $f_{\rm peak,ave}$ is an average of $f_{\rm peak}$ over the results with different grid resolutions. $f_{\rm peak}$ does not converge perfectly with respect to the grid resolution. Nonetheless, the fluctuation around the averaged value is less than 2% for a wide range of the grid resolution. This is also the case for all the binary models. Thus, we estimate a relative error due to the finite grid resolution in $f_{\rm peak}$ to be 2% and tabulate the values of $f_{\rm peak}$ in

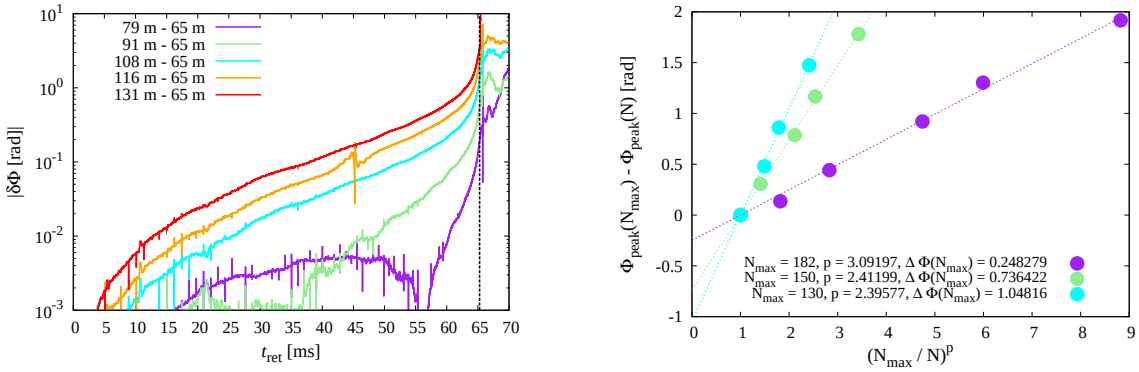

FIG. 4. (Left) Gravitational-wave phase error with respect to the grid resolution as a function of the retarded time for B107-146. The mode is the $(l, m) = (2, 2)$. The vertical dashed line denotes the peak time of the gravitational-wave amplitude with $N = 182$ (see the text for details). (Right) Gravitational-wave phase error at the peak time with a reference grid resolution denoted by $N_{\rm max}$. The purple circles show the phase error with $N_{\rm max} = 182$ and $N = 150, 130, 110, 102, 90$. The light-green color is for $N_{\rm max} = 150$ and $N = 130, 110, 102, 90$ and the cyan color is for $N_{\rm max} = 130$ and $N = 110, 102, 90$. The fitting parameters p and $\Delta\Phi(N_{\rm max})$ are listed in the legend. The purple, light-green, and cyan dashed lines denote $\Delta\Phi(N_{\rm max})[(N_{\rm max}/N)^p - 1]$ with these fitting parameters for $N_{\rm max} = 182$, 150, and 130, respectively.

Table V.

The right panel of Fig. 5 plots $f_{\rm peak}$ as a function of $\tilde{\Lambda}^{1/5}$. The error bar shows the systematics in $f_{\rm peak}$. We also plot the universal relations reported in Refs. [54] (black dashed line) and [55] (black dotted line). We find that the universal relation in Ref. [55] holds only for the symmetric binaries with $\mathcal{M}_c = 1.1752 M_\odot$ and $\mathcal{M}_c = 1.0882 M_\odot$ (see also Table V). Given an EOS and a chirp mass, $f_{\rm peak}$ shifts to a lower value as the symmetric mass ratio decreases. This is attributed to following three facts. First, given the total mass m_0 and $f_{\rm GW}$, $df_{\rm GW}/dt$ decreases as the symmetric mass ratio decreases because the gravitational-wave luminosity is proportional to η^2 [81]. Second, the time at which the two stars come into contact becomes earlier as the symmetric mass ratio decreases because the less massive companion is more subject to the tidal elongation and the resultant mass accretion on the massive component starts earlier than for the symmetric binary. Third, the time difference between the peak time and the contact time becomes small as the symmetric mass ratio decreases because the peak time corresponds to the moment when a dumbbell-like density structure with two density peaks formed after the contact disappears as discussed in Ref. [41] and the dumbbell-like density structure becomes less prominent in the asymmetric binaries. Due to these effects, $f_{\rm peak}$ becomes lower as the symmetric mass ratio decreases.

In a short summary, the $f_{\rm peak}$–$\tilde{\Lambda}^{1/5}$ relation depends strongly on the symmetric mass ratio and the universal relations reported in Refs. [54] and [55] suffer from this systematics (see also Ref. [41]). This finding is consistent with what was discussed in Ref. [55]. They mentioned the mass asymmetry could break the universality in the $f_{\rm peak}$–$\tilde{\Lambda}^{1/5}$ relation for a *possibly unrealistic* mass ratio. We find that the *realistic* value of the mass ratio breaks the universality as the symmetric mass ratio adopted in this paper is consistent with that in GW170817 [1]. The scatter from the proposed universal relation in Ref. [55] is as large as $\approx$ 18–19% at the maximum for $0.244 \le \eta \le 0.250$.

We propose an improved fitting formula:

$$\log_{10}\left[\left(\frac{f_{\rm peak}}{\rm Hz}\right)\left(\frac{m_0}{M_\odot}\right)\right] = a_0(\eta) + a_1(\eta)\tilde{\Lambda}^{1/5},$$
$$a_0(\eta) = 4.53582 - 1.22968\eta,$$
$$a_1(\eta) = -0.929178 + 3.1186\eta. \qquad (3.3)$$

With $\eta = 0.25$, $a_0(\eta)$ and $a_1(\eta)$ approximately reduce to be a_0 and a_1 [82] reported in Ref. [55]. Figure 6 plots the improved relation with the simulation data and we confirm that the relative error between the data and the fitting formula (3.3) is within 3%.

We should keep in mind that this relation may still suffer from systematics because we only explore the non-magnetized non-spinning binaries. Note that positively or negatively aligned NS spin to the orbital angular momentum could change $f_{\rm peak}$ compared to the non-spinning case because of the spin-orbit coupling. NS magnetic fields also could produce systematics in Eq. (3.3) because at the contact of the two NSs, which occurs before the peak time, the magnetic field could be exponentially amplified by the Kelvein-Helmholtz instability within a very short timescale [83, 84]. Because the magnetic pressure could reach near the equipartition of the pressure locally, its effect could be reflected in $f_{\rm peak}$. This point should be explored in a future work.

TABLE IV. Residual phase error and order of the convergence of the gravitational-wave phase at the peak time calculated by Eq. (3.1) for $N_{\rm max} = 182, 150$, and 130.

Model	$(\Delta\Phi_{\rm peak}(182), p)$	$(\Delta\Phi_{\rm peak}(150), p)$	$(\Delta\Phi_{\rm peak}(130), p)$
15H125-146	(0.11,4.1)	(0.58,2.7)	(5.44,0.7)
125H125-146	(0.31,2.6)	(0.15,4.5)	(0.45,3.6)
H125-146	(0.17,3.4)	(0.78,2.2)	(0.73,2.8)
HB125-146	(0.13,3.7)	(1.10,1.7)	(1.00,2.2)
B125-146	(0.12,3.8)	(0.28,3.7)	(0.45,3.8)
15H118-155	(0.22,3.1)	(0.75,2.2)	(0.47,3.5)
125H118-155	(0.26,2.9)	(0.83,2.1)	(1.44,1.7)
H118-155	(0.23,3.1)	(0.48,3.0)	(0.56,3.4)
HB118-155	(0.44,2.3)	(1.21,1.6)	(0.79,2.5)
B118-155	(0.29,2.7)	(0.69,2.2)	(0.47,3.3)
15H117-156	(0.26,2.9)	(0.36,3.2)	(0.39,4.0)
125H117-156	(0.28,2.8)	(0.38,2.8)	(0.92,2.4)
H117-156	(0.24,3.0)	(0.31,3.5)	(0.74,2.9)
HB117-156	(0.22,3.0)	(0.84,2.0)	(1.42,1.7)
B117-156	(0.42,2.3)	(0.43,2.8)	(0.23,4.8)
15H112-140	(0.19,3.4)	(0.70,2.5)	(0.66,3.2)
125H112-140	(0.21,3.4)	(0.53,3.0)	(0.66,3.3)
H112-140	(0.17,3.5)	(0.92,2.1)	(1.00,2.4)
HB112-140	(0.42,2.5)	(0.48,3.0)	(0.21,5.5)
B112-140	(0.19,3.6)	(0.34,3.7)	(39.59,0.13)
15H107-146	(0.38,2.6)	(0.86,2.2)	(0.43,3.9)
125H107-146	(0.54,2.2)	(2.93,1.0)	(0.61,3.2)
H107-146	(0.41,2.4)	(0.60,2.5)	(1.03,2.3)
HB107-146	(0.35,2.8)	(0.44,3.3)	(0.43,4.2)
B107-146	(0.25,3.1)	(0.73,2.4)	(1.05,2.4)
SFHo135-135	(0.43,2.3)	(0.76,2.2)	(0.33,4.2)

2. *Peak amplitude and binary tidal deformability relation*

References [41, 54] reported that the gravitational-wave amplitude at the peak time, $h_{\rm peak}$, correlates with $f_{\rm peak}$, i.e., with $\tilde{\Lambda}^{1/5}$. Because we do not find perfectly convergent result for $h_{\rm peak}$ with respect to the grid resolution, first, we assess a relative error of $h_{\rm peak}$ to an averaged value of $h_{\rm peak}$ (see for the left panel of Fig. 7 for the binaries with $m_1 = 1.07 M_\odot$ and $m_2 = 1.46 M_\odot$). It is found that fluctuation around the averaged value is $\approx$ 1–2%. This is also the case for all the binary models. Thus, we adopt 2% as the systematics in $h_{\rm peak}$ and summarize $h_{\rm peak}$ in Table V.

The right panel of Fig. 7 plots $h_{\rm peak}$ as a function of $\tilde{\Lambda}^{1/5}$. The error bar shows the systematics in $h_{\rm peak}$. This figure shows that the relation depends strongly on the symmetric mass ratio. That is, the relation proposed in Refs. [41, 54] is not satisfied in general.

We propose a fitting formula for $h_{\rm peak}$:

$$\begin{aligned} \frac{D h_{\rm peak}}{m_0} &= b_0(\eta) + b_1(\eta)\tilde{\Lambda}^{1/5}, \\ b_0(\eta) &= -0.0583284 + 1.89648\eta, \\ b_1(\eta) &= -0.160164 + 0.453901\eta. \end{aligned} \tag{3.4}$$

Figure 8 plots the improved relation with the simulation data. We find that the relative error between the data and the fitting formula (3.4) is within 4%. Again note that this relation is calibrated in a limited class of the binaries, i.e., non-magnetized non-spinning binaries. We should keep in mind this point in using this relation to infer the tidal deformability from observational data.

3. *f_1, f_2 and binary tidal deformability relation*

Reference [55] reported that several gravitational-wave frequencies associated with the main peaks in the power spectrum density correlate with the tidal coupling constant. Figures 9–11 show the power spectrum densities

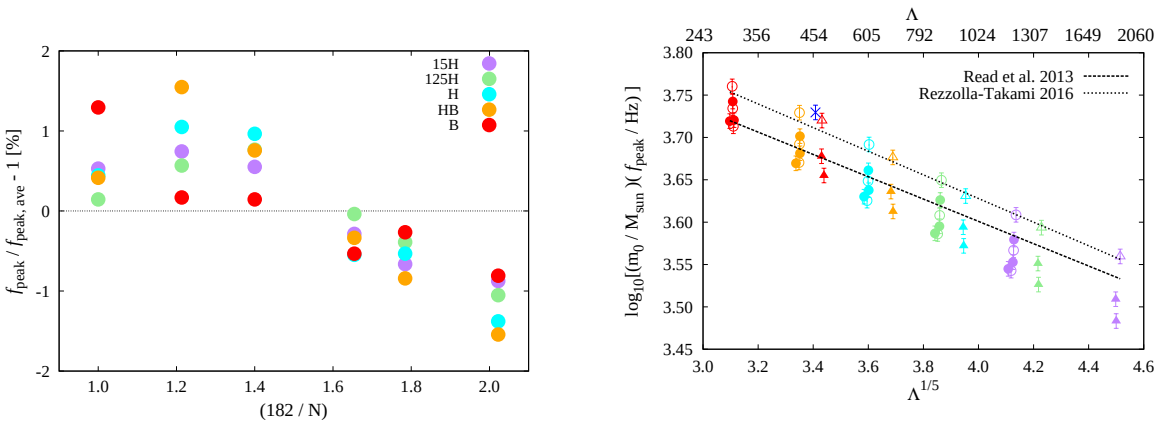

FIG. 5. (Left) Relative error of instantaneous gravitational-wave frequency at the peak time $f_{\rm peak}$ to $f_{\rm peak,ave}$ as a function of $1/N$ for the binaries with $m_1 = 1.17M_\odot$ and $m_2 = 1.56M_\odot$. $f_{\rm peak,ave}$ is an average of $f_{\rm peak}$ over the results with different grid resolutions. (Right) $f_{\rm peak}$ as a function of $\tilde{\Lambda}^{1/5}$. Meaning of the color and symbols is the same as that in Fig. 1. The error bar of $\pm 2\%$ comes from the systematics in $f_{\rm peak}$. The proposed universal relations in Refs. [54, 55] are shown.

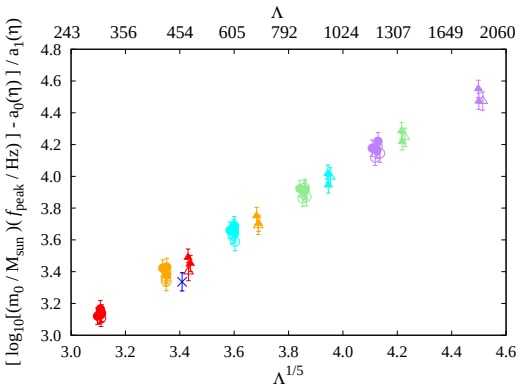

FIG. 6. An improved $f_{\rm peak}$–$\tilde{\Lambda}^{1/5}$ relation with $a_0(\eta)$ and $a_1(\eta)$ in Eq. (3.3).

of gravitational waves for all the models defined by

$$h_{\rm eff}(f) = f\sqrt{\frac{\tilde{h}_+^2(f) + \tilde{h}_\times^2(f)}{2}},$$
$$\tilde{h}_{+,\times}(f) = \int_{t_{\rm i}}^{t_{\rm f}} h_{+,\times}^{2,2,\infty}(t) e^{-2\pi i f t} dt, \qquad (3.5)$$

where $t_{\rm i}$ and $t_{\rm f}$ are the initial and final time of the waveform data, respectively. In these figures, the vertical dashed lines indicate so-called f_1 frequency for the fitting formula in Ref. [55]. Here, Ref. [55] speculated that f_1 frequency is determined by identifying one of the main peaks in the power spectrum density of gravitational waves and in the spectrogram of gravitational waves. For the symmetric binary models, f_1 peak could be identified in our numerical results. However, the structure of the power spectrum density around $f = f_1$ depends highly on the grid resolution (see 125H135-135 and H135-135 models for example). For a sequence with the fixed EOS and chirp mass, e.g., 15H135-135, 15H125-146, 15H121-151, 15H118-155, 15H117-156, and 15H116-158, it becomes difficult to identify f_1 peak as the symmetric mass ratio decreases. This was also pointed out in Ref. [85]. However, their grid resolution is much lower than those in our present study and the resolution study on the power spectrum density of gravitational waves has not been performed (see their Fig. 13). Thus, it was not conclusive whether f_1 peak is less prominent for the asymmetric binaries or not. As demonstrated in Figs. 9 and 10, f_1 peak cannot be clearly identified for the asymmetric binaries.

For the less massive symmetric binaries, there is a discussion how to identify f_1 frequency in the power spectrum density and/or in the spectrogram of gravitational waves [55, 86, 87]. Figures 9–11 demonstrate that the identification of f_1 frequency is a subtle issue because a fine structure of the power spectrum density around $f = f_1$ depends strongly on the grid resolution and the EOSs even for the symmetric binaries.

We also analyze the spectrogram of gravitational waves and confirm that there is no prominent peak around $f_{\rm GW} = f_1$. Therefore, we conclude that the universal relation for f_1 could be only applicable to nearly symmetric binaries: essentially no universal relation is present.

In Ref. [55], the peak frequency, f_2, in the power spectrum density is reported to have a correlation with the tidal coupling constant. This peak frequency approximately corresponds to the f–mode oscillation of the remnant massive NS (see also Refs. [45, 60, 80, 88]). The left panel of Fig. 12 plots fluctuation around an averaged value of f_2 for the binaries with $m_1 = 1.12M_\odot$ and $m_2 = 1.40M_\odot$. The fluctuation is within ≈ 4–5% and we find that this is also the case for all the binary models.

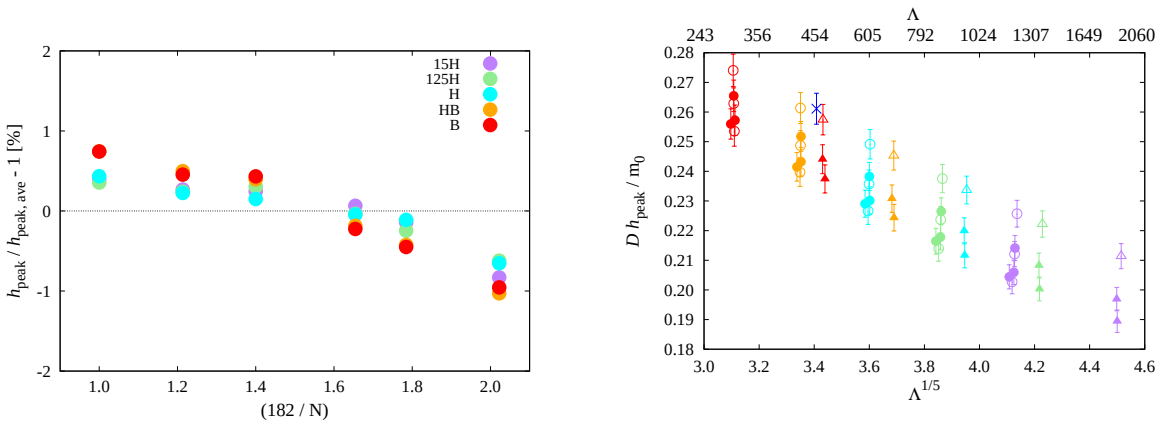

FIG. 7. (Left) Relative error of the gravitational-wave amplitude at the peak time, $h_{\rm peak}$, to $h_{\rm peak,ave}$ as a function of $1/N$ for the binaries with $m_1 = 1.07M_\odot$ and $m_2 = 1.46M_\odot$. $h_{\rm peak,ave}$ is an average of $h_{\rm peak}$ over the results with different grid resolutions. (Right) $h_{\rm peak}$ as a function of $\tilde{\Lambda}^{1/5}$. Meaning of the color and symbols is the same as Fig. 1. The error bar of $\pm 2\%$ comes from the uncertainty in $h_{\rm peak}$.

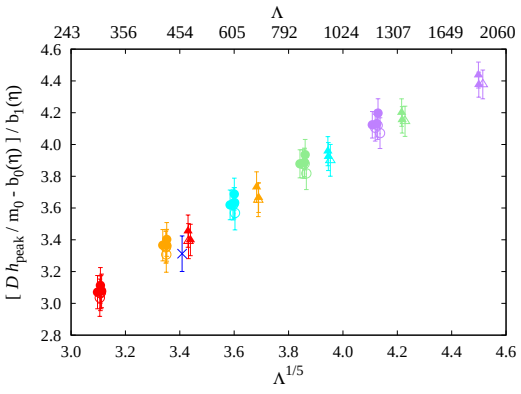

FIG. 8. An improved $h_{\rm peak}$–$\tilde{\Lambda}^{1/5}$ relation with $b_0(\eta)$ and $b_1(\eta)$ in Eq. (3.4).

Thus, we adopt 5% as a relative error in f_2 (see also Table V). The right panel of Fig. 12 shows f_2 as a function of $\tilde{\Lambda}^{1/5}$. We exclude the models which collapse to a black hole within a few ms after merger because the peak associated with f_2 is not prominent or absent in the power spectrum density. We also overplot the fitting formula proposed in Ref. [55]. With it, the scatter is $\approx 14\%$ at the maximum. We propose an improved fitting formula for f_2;

$$\log_{10}\left[\left(\frac{f_2}{\rm Hz}\right)\left(\frac{m_0}{M_\odot}\right)\right] = c_0(\eta) + c_1(\eta)\tilde{\Lambda}^{1/5},$$
$$c_0(\eta) = 11.3634 - 27.4181\eta,$$
$$c_1(\eta) = -2.15771 + 7.94086\eta \qquad (3.6)$$

Even with this formula, the relative error is within 9% (see also Fig. 13).

4. f_2 and NS radius with $1.6M_\odot$ relation

References [59, 60] reported that f_2 frequency [89] has a tight correlation with the NS radius of $1.6M_\odot$ (see Eq. (3) in Ref. [59]). In Ref. [80], we assessed their relation by using our numerical-relativity results and found that the scatter in the relation is larger than that reported in Ref. [59]. This could stem from the different treatment of the relativistic gravity, i.e., the conformal flat approximation in Ref. [59] and the full general relativity in Ref. [80], and/or the different method for the relativistic hydrodynamics, i.e., the smoothed particle hydrodynamics in Ref. [59] and the high resolution shock capturing scheme in Ref. [80]. We revisit this assessment because the initial orbital eccentricity reduction was not implemented in Ref. [80]. In addition, the grid resolution in Ref. [80] is much lower than that in this paper. Updates of these ingredients could modify the post-merger dynamics and the resulting gravitational waveforms.

Because the relation in Ref. [59] holds only for $m_0 = 2.7M_\odot$ binaries, we assess this relation by employing $(m_1, m_2) = (1.35M_\odot, 1.35M_\odot)$, $(1.25M_\odot.1.46M_\odot)$, $(1.21M_\odot, 1.51M_\odot)$, $(1.18M_\odot, 1.55M_\odot)$, $(1.17M_\odot, 1.56M_\odot)$, and $(1.16M_\odot, 1.58M_\odot)$ binaries. We found the scatter from their fitting formula is $\approx 10\%$. Therefore, the scatter larger than that in Ref. [59] exits. Our numerical results suggest that even if the value of f_2 is determined precisely, we cannot constrain the radius of the $1.6M_\odot$ NS within the 1 km accuracy.

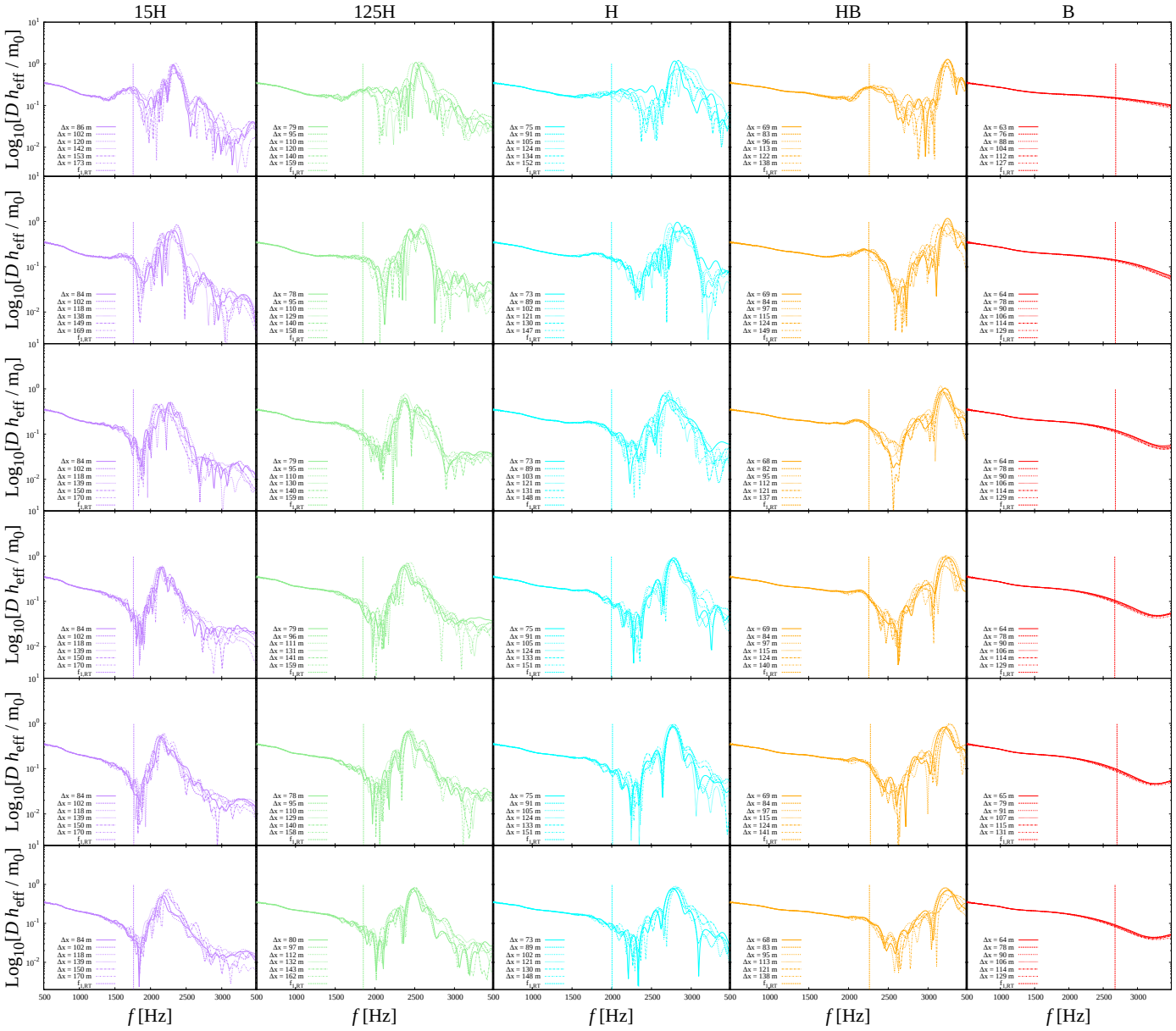

FIG. 9. Power spectrum densities of gravitational waves for the binaries with $\mathcal{M}_c = 1.1752 M_\odot$. The number attached in the right-hand side vertical axis is the symmetric mass ratio η. We also show f_1 frequency proposed in Ref. [55] with vertical dashed lines. For completeness, we also show the models reported in Refs. [41, 42].

D. Energy and angular momentum dissipation due to gravitational wave emission

Using Eqs. (2.10) and (2.11), we calculate the energy and angular momentum carried by gravitational waves. We define $E^{\rm tot}_{\rm GW,i}$ and $E_{\rm GW,p}$ ($J_{\rm GW,p}$) as the energy (angular momentum) emitted in the inspiral stage and in the post-merger stage, respectively. The peak time introduced in Sec. III A defines the boundary between the inspiral and post-merger stages. In the following we summarize the energy and angular momentum emitted in each stage for all the models in Table V.

1. *inspiral stage*

Table V and Fig. 14 show the energy, $E^{2,2}_{\rm GW,i}$, carried by gravitational waves with the $(l,m)=(2,2)$ mode during the simulations. A perfect convergence with respect to the grid resolution in this quantity is not achieved. We measure a relative error with respect to an averaged value in the left panel of Fig. 14. It is encouraging that the relative error to its averaged value of $E^{2,2}_{\rm GW,i}$ never exceeds

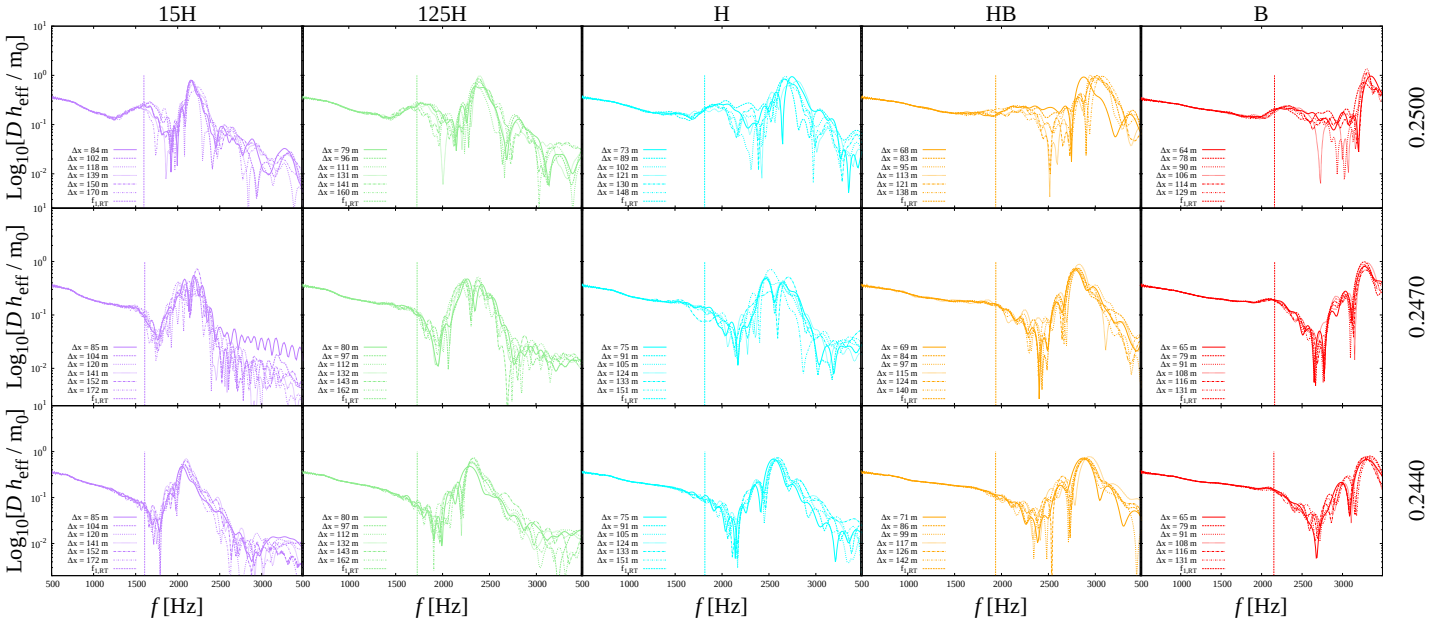

FIG. 10. The same as Fig. 9, but for the binaries with $\mathcal{M}_c = 1.0882 M_\odot$.

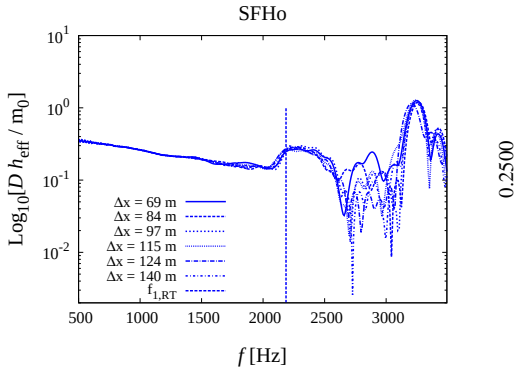

FIG. 11. The same as Fig. 9, but for the SFHo (tabulated) EOS case.

2% for a wide range of the grid resolution. This is also the case for all the binary models. Thus, we adopt this fluctuation as an error in $E^{2,2}_{\rm GW,i}$.

The right panel of Fig. 14 plots $E^{\rm tot}_{\rm GW,i}$ as a function of $\tilde{\Lambda}^{1/5}$. Note that the contributions in $E^{\rm tot}_{\rm GW,i}$ from the other modes such as the $(l,m) = (2,1)$ and $(3,3)$ are $\lesssim 0.1\%$ and $\lesssim 0.5\%$, respectively, of $E^{2,2}_{\rm GW,i}$. We include the contribution due to the gravitational-wave emission during evolution from infinite separation to the initial orbital separation of the simulation, $m_0 - M_{\rm ADM}$ in Table V, by $E^{\rm tot}_{\rm GW,i} \approx E^{2,2}_{\rm GW,i} + E^{2,-2}_{\rm GW,i} + m_0 - M_{\rm ADM} = 2E^{2,2}_{\rm GW,i} + m_0 - M_{\rm ADM}$. As proposed in Ref. [56], this quantity correlates with the tidal coupling constant. We explicitly derive a fitting formula with the binary tidal deformability;

$$\log_{10}\left[\frac{E^{\rm tot}_{\rm GW,i}}{c^2 m_0 \eta}\right] = -0.8688062 - 0.11099\tilde{\Lambda}^{1/5}. \qquad (3.7)$$

The dependence of $E^{\rm tot}_{\rm GW,i}$ on $\tilde{\Lambda}$ is satisfied because the binaries with larger values of $\tilde{\Lambda}$ merge earlier than those with smaller values of $\tilde{\Lambda}$. This fitting formula reproduces the simulation data of $E^{\rm tot}_{\rm GW,i}$ within an error of $\approx 4\%$.

2. *Post-merger stage*

We estimate the angular momentum of the remnant, $J_{\rm rem}$, by performing a surface integral on the sphere of $r = r_0$ at the peak time of the gravitational-wave amplitude in the retarded time (2.4);

$$J_{\rm rem} = \frac{1}{8\pi}\epsilon^{zjk}\oint_{r=r_0} x_j (K^l{}_k - K\delta^l{}_k) dS_l, \qquad (3.8)$$

where j and k denote x or y. K_{ij}, K, and $\delta^i{}_j$ are the extrinsic curvature, its trace part, and the Kronecker delta, respectively. We typically integrate it on the sphere of $r_0 = 200m_0$ and $214m_0$ for the binaries with $\mathcal{M}_c = 1.1752 M_\odot$ and $1.0882 M_\odot$, respectively. Table V and Fig. 15 show the angular momentum of the remnant. In the left panel of Fig. 15, we estimate the residual error in $J_{\rm rem}$ for HB118–155. We again assume that the

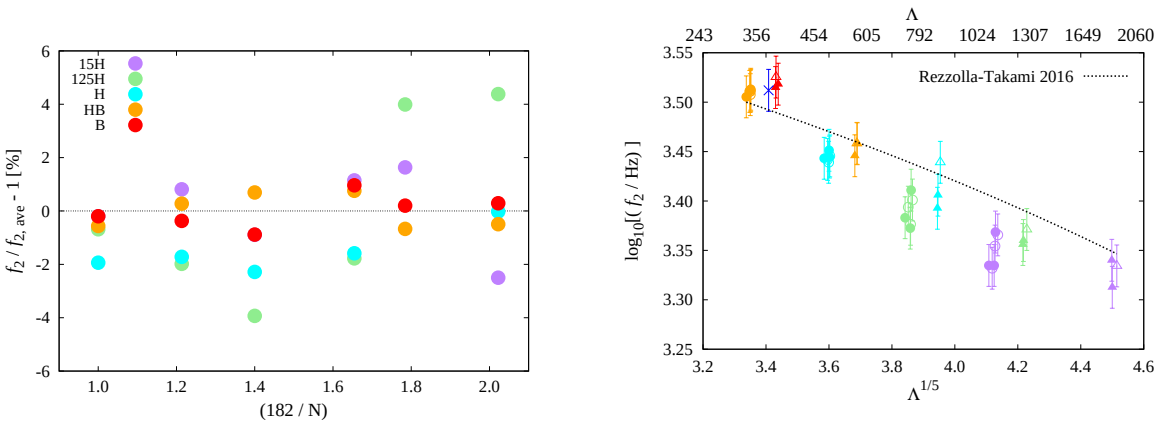

FIG. 12. (Left) Relative error of f_2 frequency in the power spectrum density to $f_{2,\rm ave}$ as a function of $1/N$ for the binaries with $m_1 = 1.12 M_\odot$ and $m_2 = 1.40 M_\odot$. $f_{2,\rm ave}$ is an average of f_2 over the results with different grid resolutions. (Right) f_2–$\tilde{\Lambda}^{1/5}$ relation for the binaries except for those which collapse to a black hole within a few ms after merger. The error bar of ±5% comes from the systematics in f_2.

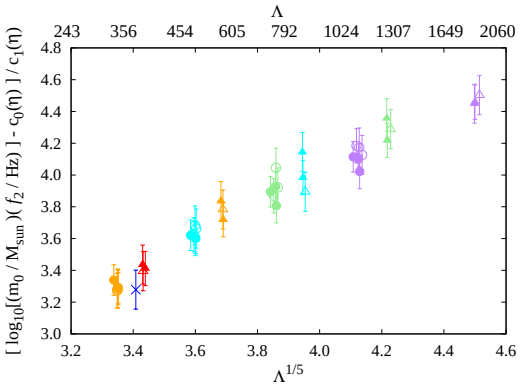

FIG. 13. An improved f_2–$\tilde{\Lambda}^{1/5}$ relation with $c_0(\eta)$ and $c_1(\eta)$ in Eq. (3.6).

numerical result obeys a following form;

$$J_{\rm rem}(N) = J^{\infty}_{\rm rem}(N_{\rm max}) - \Delta J_{\rm rem}(N_{\rm max}) \left(\frac{N_{\rm max}}{N}\right)^p. \tag{3.9}$$

We estimate three unknowns, $J^{\infty}_{\rm rem}(N_{\rm max})$, $\Delta J_{\rm rem}(N_{\rm max})$, and p by fitting the numerical data with $N = 90, 102, \cdots$, and $N_{\rm max}$ with Eq. (3.9). By comparing $N_{\rm max} = 150$ and 182 cases, we confirm that adding a result of the higher resolution simulation reduces the residual error (see the legend of Fig. 15 for p and $\Delta J_{\rm rem}(N_{\rm max})$). We find that $\Delta J_{\rm rem}(N_{\rm max})$ is $\lesssim 1\%$ of the continuum limit $J^{\infty}_{\rm rem}(N_{\rm max})$ for $N_{\rm max} = 182$. This is also the case for all the binary models. We adopt this value 1% as a systematics in $J_{\rm rem}$.

Because $J_{\rm rem}$ is likely to correlate with $\tilde{\Lambda}^{1/5}$, we propose a fitting formula of $J_{\rm rem}$:

$$\begin{aligned} \log_{10}\left[\frac{G J_{\rm rem}}{c m_0^2 \eta}\right] &= d_0(\eta) + d_1(\eta)\tilde{\Lambda}^{1/5}, \\ d_0(\eta) &= 1.5521 - 4.27546\eta, \\ d_1(\eta) &= -0.14137 + 0.64231\eta. \end{aligned} \tag{3.10}$$

The right panel of Fig. 15 plots $J_{\rm rem}$ as a function of $\tilde{\Lambda}^{1/5}$ and we confirm that this fitting formula is accurate within 3% error.

Figures 16 and 17 plot $E^{2,2}_{\rm GW,p}$ and $J^{2,2}_{\rm GW,p}$ emitted in the post-merger stage. The left panels in these figures show that it is hard to achieve a perfect convergence and the scatter is rather large compared to $E^{2,2}_{\rm GW,i}$. Nonetheless, the scatter never exceeds 50% in $E^{2,2}_{\rm GW,p}$ and $J^{2,2}_{\rm GW,p}$. This is also the case for all the binary models. The right panels in Figs. 16 and 17 show $E^{2,2}_{\rm GW,p}$ and $J^{2,2}_{\rm GW,p}$ as a function of $\tilde{\Lambda}^{1/5}$. As discussed in Ref. [58], the energy and angular momentum radiated in the post-merger stage peak around $\tilde{\Lambda} \approx 400$ because the binaries with $\tilde{\Lambda} \lesssim 350$ collapse to a black hole within a few ms after the peak time. However, $\tilde{\Lambda}$ at the peak in $E^{2,2}_{\rm GW,p}$ and $J^{2,2}_{\rm GW,p}$ could decrease for general EOSs because as discussed in Ref. [92] the remnant would survive longer than 20 ms after the peak time even for the binaries with $\tilde{\Lambda} \lesssim 300$. For $\tilde{\Lambda} \gtrsim 400$, correlation between $E^{2,2}_{\rm GW,p}$ and the binary tidal deformability is not as tight as that in $E^{\rm tot}_{\rm GW,i}$–$\tilde{\Lambda}^{1/5}$. For $J^{2,2}_{\rm GW,p}$, the correlation with the binary tidal deformability is also not so tight. Note that $E^{2,2}_{\rm GW,p}$ and $J^{2,2}_{\rm GW,p}$ could increase from the values listed in Table V because we artificially terminated the simulations at 10–15 ms after the peak time. At that moment, the gravitational-wave amplitude is still comparable to that in the late inspiral stage except for the models which collapse to a black hole within a few ms after the peak time.

We should also keep in mind that we could miss relevant physics such as effective turbulent viscosity generated by the magneto-hydrodynamical instabilities during the merger [41, 83, 84] and/or the neutrino cooling [86, 93] for modeling the post-merger signal. Reference [94] suggests that the post-merger signal could be significantly suppressed in the presence of efficient angular momentum transport by the viscous effect inside the remnant NS. It is worth noting that energy and angular momentum radiated by gravitational waves in the $(l,m)=(2,1)$ and $(3,3)$ modes are $\lesssim 2.5\%$ of $E^{2,2}_{\rm GW,p}$ and $\lesssim 2.4\%$ of $J^{2,2}_{\rm GW,p}$, respectively, even for highly asymmetric binaries, e.g., 15H107-146.

Post-merger gravitational wave signal is dominated by the f–mode oscillation with $(l,m)=(2,2)$ of the remnant massive NS [60, 80]. Thus, it is natural to expect that a relation holds between the energy emission rate and angular momentum emission rate (2.10) with instantaneous gravitational-wave frequency (2.9);

$$\frac{dE_{\rm GW,p}}{dt} \approx \pi f_{\rm GW} \frac{dJ_{\rm GW,p}}{dt}, \tag{3.11}$$

where $dE_{\rm GW,p}/dt = \sum_{l,m} dE^{l,m}_{\rm GW,p}/dt$ and $dJ_{\rm GW,p}/dt = \sum_{l,m} dJ^{l,m}_{\rm GW,p}/dt$. To investigate to what extent this relation is satisfied, we generate Figs. 18–20. In these figures, the solid curve is the left hand side of Eq. (3.11) and the dashed curve is the right hand side of Eq. (3.11). We find that they agree with each other with a relative error $\lesssim 8\%$. Because the emissivity reduces quickly to zero at $t_{\rm ret}-t_{\rm peak}\approx 0.5$ ms as shown in Figs. 18–20, we estimate the error for $t_{\rm ret}-t_{\rm peak}\gtrsim 1$ ms. We also find that the time integrated values of Eq. (3.11) agree with each other with a relative error $\lesssim 1\%$. This is also the case for the relation of $E_{\rm GW,p}\approx \pi f_2 J_{\rm GW,p}$. In the top panel of Fig. 21, we plot the energy flux for the $(l,m)=(2,2)$, $(2,1)$, and $(3,3)$ modes for 15H107-146. For the entire post-merger stage in the simulations, the energy flux with the $(l,m)=(2,1)$ and $(3,3)$ modes are $\lesssim 4\%$ of that with the $(l,m)=(2,2)$ mode even for highly asymmetric binaries. We find that this is also the case for the angular momentum flux. We also confirm that a contribution from the one-arm spiral instability in the post-merger stage [95, 96] is very small because the energy flux for $(l,m)=(2,1)$ mode is $\lesssim 0.5\%$ of that for the $(l,m)=(2,2)$ mode for symmetric binaries as shown in the bottom panel of Fig. 21. Thus, we conclude that Eq. (3.11) is nicely satisfied and confirm that the main gravitational-wave emission mechanism during the post-merger stage is the f–mode oscillation of the remnant massive NS, i.e, $f_{\rm GW}\approx f_2$ (see also Figs. 9–11). These findings encourage us to build a model for the post-merger gravitational-wave emission (see Ref. [91]).

In Table VI, we summarize to what extent the so-called universal relations hold.

IV. GRAVITATIONAL WAVEFORM MODELING

A. SACRA gravitational waveform template

In the previous paper [42], we developed a frequency-domain gravitational waveform model for inspiralling BNSs based on high-precision numerical-relativity data. In this section, we extend the examination of the waveform model to a wider parameter space than the previous papers [41, 42] by employing new numerical-relativity waveforms obtained in this paper.

Before moving on to the comparison, we briefly review our waveform model. We decompose $\tilde{h}(f) \equiv \sqrt{\tilde{h}_+^2(f)+\tilde{h}_\times^2(f)}$ in Eq. (3.5) into the frequency-domain amplitude, $A(f)$, and phase, $\Phi(f)$, (with an ambiguity in the origin of the phase) by

$$\tilde{h}(f) = A(f)\, {\rm e}^{-i\Phi(f)}, \tag{4.1}$$

and we define the corrections due to the NS tidal deformation to gravitational-wave amplitude and phase by

$$A_{\rm tidal}(f) = A(f) - A_{\rm BBH}(f) \tag{4.2}$$

and

$$\Phi_{\rm tidal}(f) = \Phi(f) - \Phi_{\rm BBH}(f), \tag{4.3}$$

respectively. Here, $A_{\rm BBH}(f)$ and $\Phi_{\rm BBH}(f)$ are the gravitational-wave amplitude and phase of a binary black hole with the same mass as the BNS, respectively (hereafter referred to as the point-particle parts and see Ref. [42] for details).

Our numerical-relativity waveforms only contain the waveforms for the frequency larger than ≈ 400 Hz. Thus, we employ the effective-one-body waveforms of Refs. [97–99] (SEOBNRv2T) to model the low-frequency part waveforms, in which the effect of dynamical tides is taken into account, and construct hybrid waveforms combining them with the numerical-relativity waveforms. The hybridization of the waveforms is performed in the time-domain by the procedure described in Refs. [42, 48] and we set the matching region to be from $t_{\rm ret}\approx 7.38$ ms to 14.78 ms. After the hybridization, the waveforms are transformed into the frequency domain employing Eq. (3.5), and the tidal-part amplitude and phase are extracted by Eqs. (4.2) and (4.3).

For modeling the tidal-part phase and amplitude, we employ the following functional forms motivated by the 2.5 PN order formula [49]:

$$\Phi^{\rm tidal}_{\rm model} = \frac{3}{128\eta}\left[-\frac{39}{2}\tilde{\Lambda}\left(1+a\,\tilde{\Lambda}^{2/3}x^p\right)\right]x^{5/2} \times\left(1+\frac{3115}{1248}x-\pi x^{3/2}+\frac{28024205}{3302208}x^2-\frac{4283}{1092}\pi x^{5/2}\right) \tag{4.4}$$

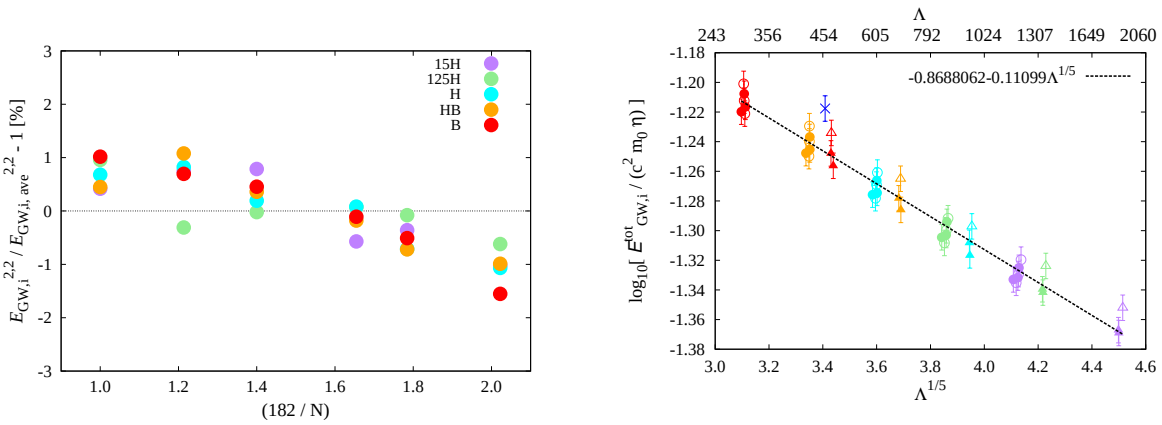

FIG. 14. (Left) Relative error of $E^{2,2}_{\rm GW,i}$ to $E^{2,2}_{\rm GW,i,ave}$ as a function of $1/N$ for binaries with $m_1 = 1.25M_\odot$ and $m_2 = 1.46M_\odot$. $E^{2,2}_{\rm GW,i,ave}$ is an average of $E^{2,2}_{\rm GW,i}$ over the results with different grid resolutions. (Right) $E^{\rm tot}_{\rm GW,i}$–$\tilde{\Lambda}^{1/5}$ relation with a fitting formula (3.7). In the right panel, the error bar of $\pm 2\%$ comes from the systematics in $E^{2,2}_{\rm GW,i}$.

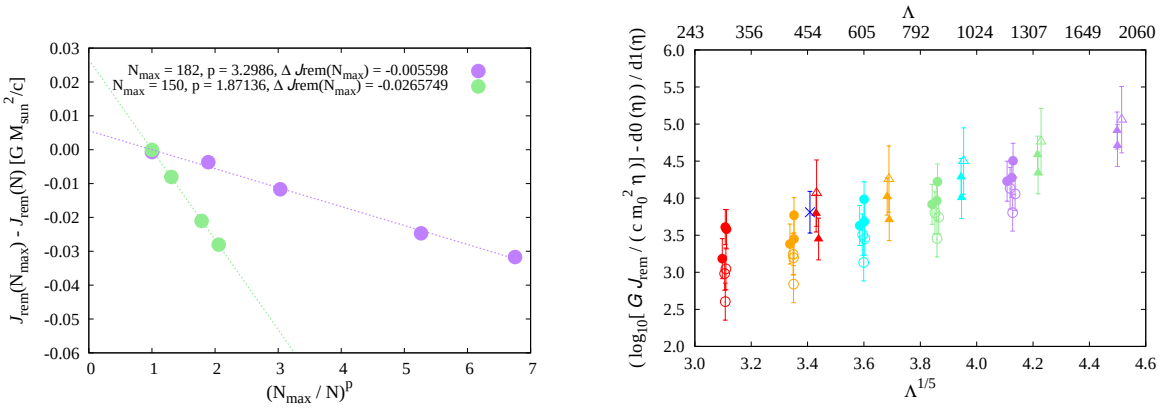

FIG. 15. (Left) Convergence of $J_{\rm rem}$ with respect to the grid resolution for HB118–156. (Right) $J_{\rm rem}$–$\tilde{\Lambda}^{1/5}$ relation with $d_0(\eta)$ and $d_1(\eta)$ in Eq. (3.10). The error bar of $\pm 1\%$ comes from the systematics in $J_{\rm rem}$.

for the phase correction and

$$A^{\rm tidal}_{\rm model} = \sqrt{\frac{5\pi\eta}{24}}\frac{m_0^2}{D_{\rm eff}}\tilde{\Lambda}x^{-7/4} \times\left(-\frac{27}{16}x^5 - \frac{449}{64}x^6 - b\,x^q\right) \qquad (4.5)$$

for the amplitude correction. a, p, b, and q are the free parameters of the models. To focus on the inspiral-phase waveform and to avoid the contamination from the post-merger waveforms, which would have large uncertainties, we restrict the gravitational-wave frequency range in 10–1000 Hz. The fitting parameters were determined by employing the hybrid waveforms of 15H125-125, which has the largest value of binary tidal deformability in the models studied in the previous study [42]. By performing the least square fit with respect to the phase shift and relative difference of the amplitude, we obtained $a = 12.55$, $p = 4.240$, $b = 4251$, and $q = 7.890$.

In Ref. [42], the validity of the waveform model was examined employing hybrid waveforms which were not used for the parameter determination. We should stress again that the parameters a, p, b, and q in Eqs. (4.4)–(4.5) were determined by the particular model 15H125-125. We found that the tidal-part waveform model always reproduced the tidal-part phase and amplitude of the hybrid waveforms within ~ 0.1 radian and 15%, respectively, for the equal-mass and unequal-mass cases with $\mathcal{M}_{\rm chirp} = 1.1752\,M_\odot$ and the equal-mass cases with $\mathcal{M}_{\rm chirp} = 1.0882\,M_\odot$, covering the parameter space of $0.244 \le \eta \le 0.250$ and $300 \lesssim \tilde{\Lambda} \lesssim 1800$.

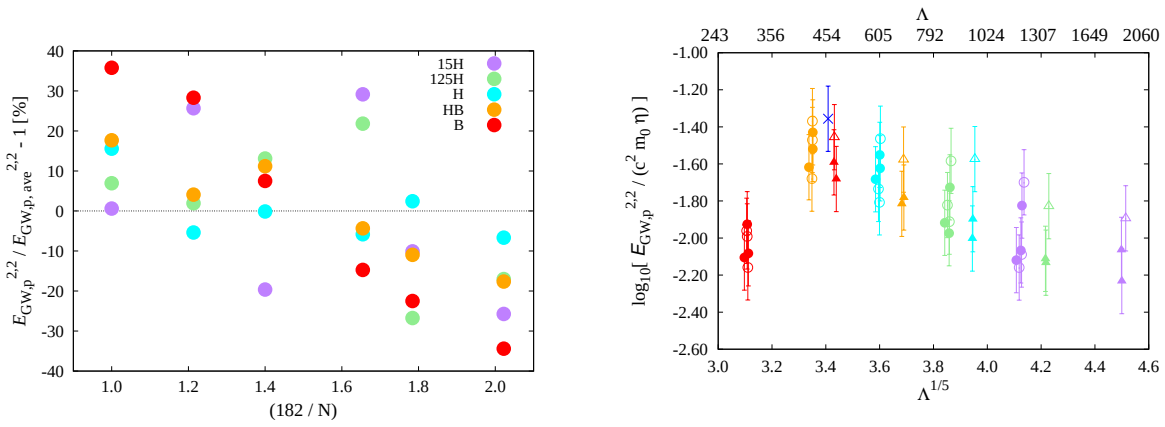

FIG. 16. (Left) Relative error of $E^{2,2}_{\rm GW,p}$ to $E^{2,2}_{\rm GW,p,ave}$ as a function of $1/N$ for binaries with $m_1 = 1.25M_\odot$ and $m_2 = 1.46M_\odot$. $E^{2,2}_{\rm GW,p,ave}$ is an average of $E^{2,2}_{\rm GW,p}$ over the results with different grid resolutions. (Right) $E^{2,2}_{\rm GW,p}$–$\tilde{\Lambda}^{1/5}$ relation. In the right panel, the error bar of $\pm 50\%$ comes from the systematics in $E^{2,2}_{\rm GW,p}$.

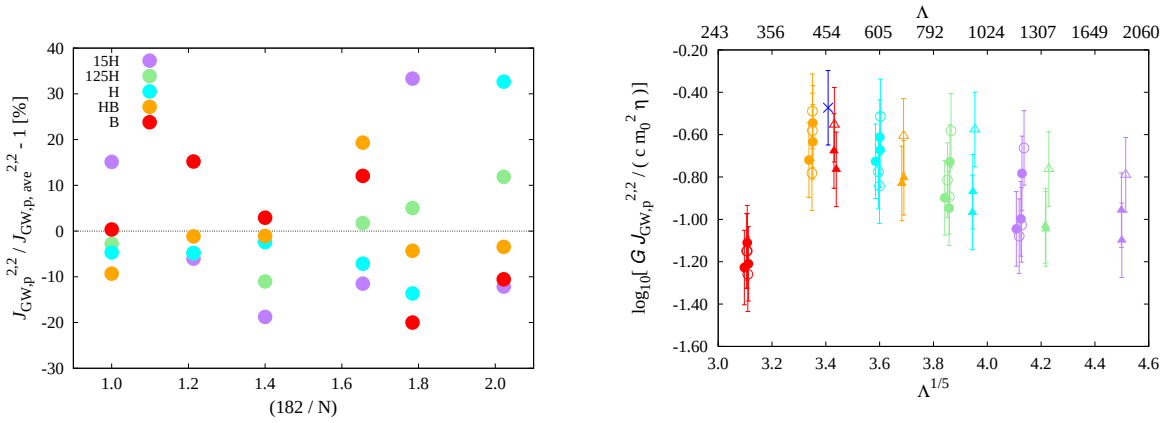

FIG. 17. The same as Fig. 16, but for $J^{2,2}_{\rm GW,p}$. The left panel is for the binaries with $m_1 = 1.12M_\odot$ and $m_2 = 1.40M_\odot$.

B. Calibration of SACRA gravitational waveform template

While the validity of our waveform was already examined in the most interesting part of the parameter space of BNSs [42], there still remain some important cases which are not examined in the previous study [42]. First, the dependence of the error of the tidal correction on the mass ratio has to be checked for less massive BNSs. While unequal-mass cases with total mass of $\approx 2.7\,M_\odot$ were checked in the previous study [42], it is important to check whether our waveform models are also applicable to unequal-mass cases with smaller total mass, for which the tidal effect is enhanced due to increase of tidal deformability. Second, the systematics due to simplification on the high-density part of the EOS should be checked. For the inspiral waveforms, we expect that the high-density part of the EOS has only a minor effect, and accordingly, we employ simplified two piece-wise polytropic EOS models. However, we should confirm that this assumption is indeed valid.

To check the points listed above, we compare our waveform model with hybrid waveforms employing the numerical-relativity waveforms obtained in this paper. Hybrid waveforms are constructed in the same manner as in the previous study [42] employing the SEOBNRv2T waveforms as the low-frequency part waveforms. In particular, we focus on the validity of the tidal correction model to the waveform, comparing the tidal-part phase and amplitude of the hybrid waveforms computed based on Eqs. (4.2) and (4.3) using the SEOBNRv2 waveforms without tides as the point-particle parts.

Figures 22 and 23 show the difference of the tidal-part phase and amplitude between our waveform model (4.4) and (4.5) and the hybrid waveforms for the models

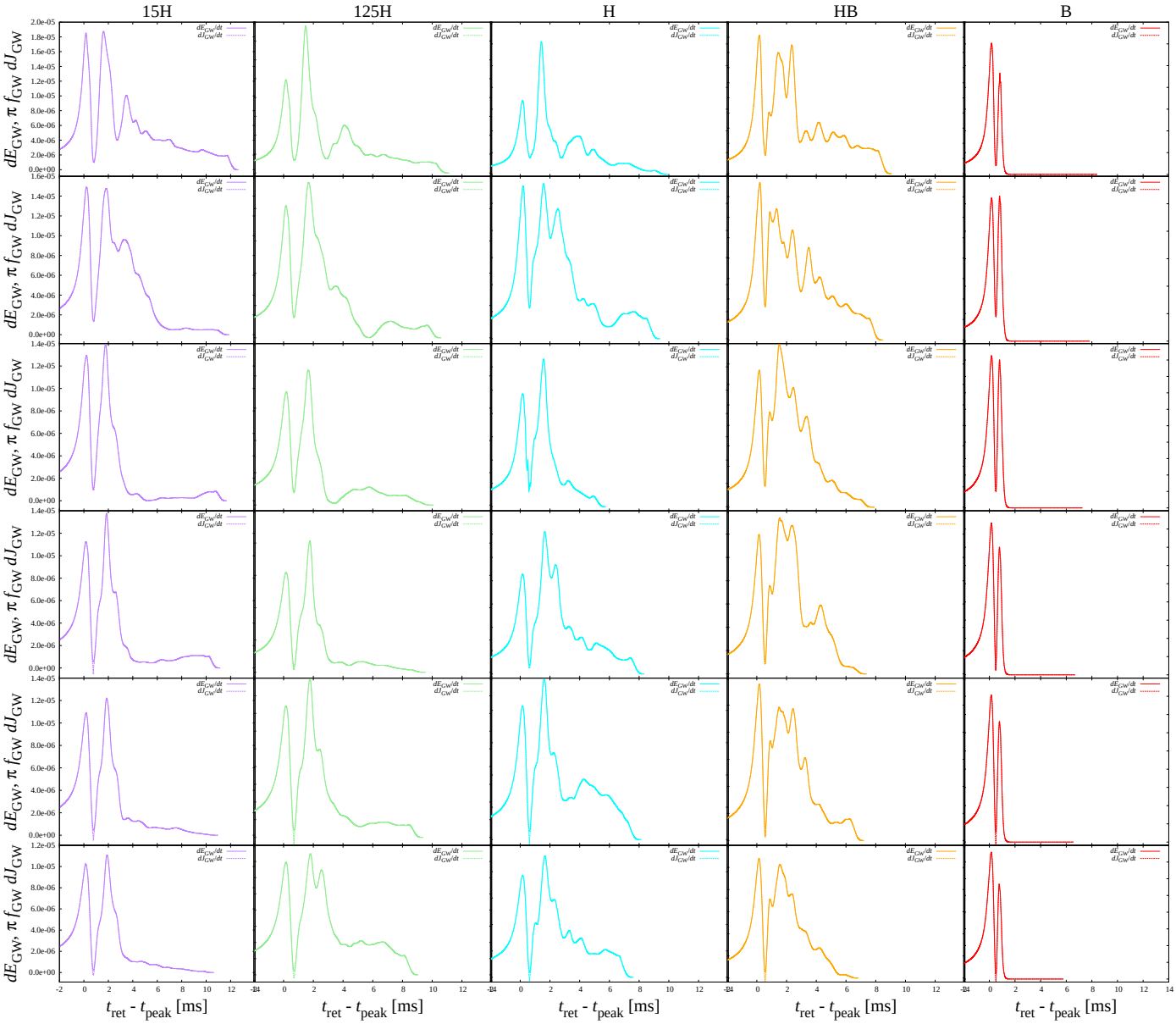

FIG. 18. Energy (solid) and angular momentum (dashed) emission rate by gravitational waves (3.11) for the binaries with $\mathcal{M}_c = 1.1752 M_\odot$. The time axis is set to be zero at the peak time of the gravitational-wave amplitude. For completeness, we also show the models reported in Refs. [41, 42].

with $\mathcal{M}_c = 1.1752\,M_\odot$ and $\mathcal{M}_c = 1.0882\,M_\odot$, respectively. Here, the difference between the tidal-part phase of hybrid waveforms, $\Phi^{\rm tidal}_{\rm Hybrid}$, and that of our waveform model, $\Phi^{\rm tidal}_{\rm model}$, is computed by

$$\Delta\Phi(f) = \Phi^{\rm tidal}_{\rm Hybrid}(f) - \Phi^{\rm tidal}_{\rm model}(f) - 2\pi f t_0 + \phi_0, \quad (4.6)$$

where t_0 and ϕ_0 are the free parameters which correspond to the degrees of freedom in choosing the origins of time and phase, respectively, and are determined by minimizing $\int |\Delta\Phi(f)|^2 df$ integrated in the range of $f = 10$–1000 Hz. For the comparison of the tidal-part amplitude, relative difference of the amplitude,

$$\Delta A(f)/A(f) = (A^{\rm tidal}_{\rm Hybrid}(f) - A^{\rm tidal}_{\rm model}(f))/A_{\rm model}(f), \quad (4.7)$$

is computed, where $A^{\rm tidal}_{\rm Hybrid}$ and $A_{\rm model} = A^{\rm tidal}_{\rm model} + A_{\rm BBH}$ are the tidal-part amplitude of hybrid waveforms and the amplitude of the model waveforms including the point-particle part, respectively.

NS masses for the models 125-146, 118-155, and 117-156 are within the parameter space which we studied in the previous study [42], and thus, we expect that these

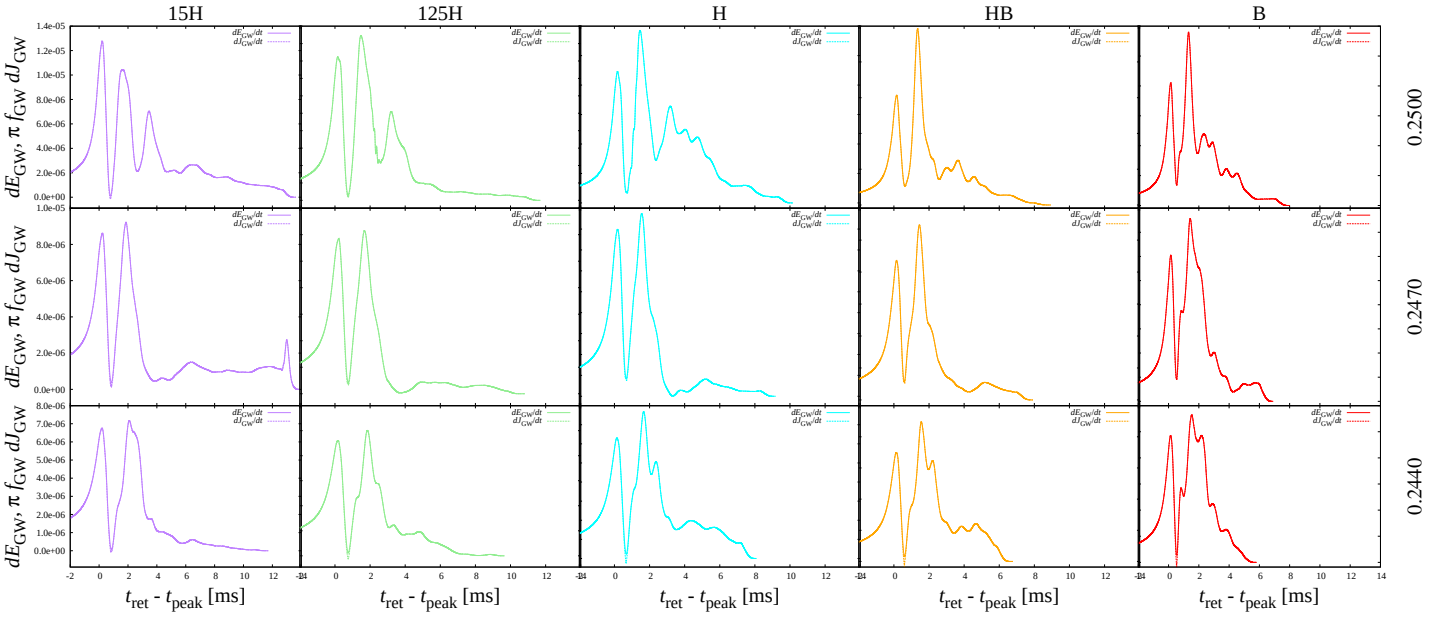

FIG. 19. The same as Fig. 18, but for $\mathcal{M}_c = 1.0882 M_\odot$.

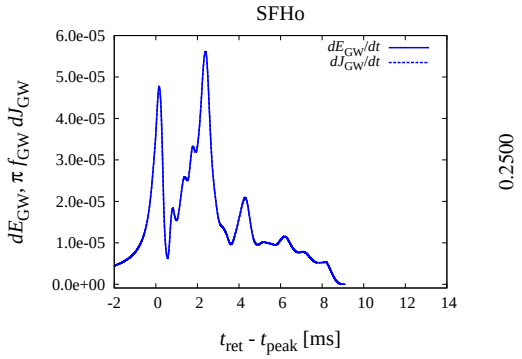

FIG. 20. The same as Fig. 18, but for the SFHo (tabulated) EOS case.

waveforms are well reproduced by our waveform model. Indeed Fig. 22 shows that differences in both phase and amplitude are within the error which we observed in the previous study [42]. Figure 22 also shows that tidal-part phase and amplitude for model SFHo135-135 are well reproduced by our waveform model. This confirms that, at least for the frequency range we focus on, employing an EOS whose high-density part is simplified has only a minor effect on the systematics of the model. Figure 23 shows the results in the unequal-mass cases with $\mathcal{M}_c = 1.0882\, M_\odot$. The difference in the tidal-part phase is relatively larger than the cases with $\mathcal{M}_c = 1.1752\, M_\odot$. This is reasonable because we found that the error of tidal-part model becomes relatively large for a small mass ratio or a large value of tidal deformability in the previous study [42]. Nevertheless, the phase error is always smaller than ≈ 0.1 radian. The deviation for the amplitude model is also the same level as for the models with $\mathcal{M}_c = 1.1752\, M_\odot$.

To evaluate the deviation for the waveform model from the new sets of hybrid waveforms more quantitatively, we calculate the mismatch between those waveforms, $\bar{F}$, defined by

$$\bar{F} = 1 - \max_{\phi_0, t_0} \frac{\left(\tilde{h}_1 \middle| \tilde{h}_2 e^{2\pi i f t_0 + i\phi_0}\right)}{||\tilde{h}_1||\, ||\tilde{h}_2||}, \tag{4.8}$$

where $(\cdot|\cdot)$ and $||\cdot||$ are defined by

$$\left(\tilde{h}_1 \middle| \tilde{h}_2\right) = 4\mathrm{Re}\left[\int_{f_{\min}}^{f_{\max}} \frac{\tilde{h}_1(f)\, \tilde{h}_2^*(f)}{S_n(f)} df\right], \tag{4.9}$$

and

$$||\tilde{h}|| = \sqrt{\left(\tilde{h} \middle| \tilde{h}\right)}. \tag{4.10}$$

Here S_n denotes the one-sided noise spectrum density of the detector, and we employ the noise spectrum density of the `ZERO_DETUNED_HIGH_POWER` configuration of advanced LIGO [100] for it.

We summarize the values of mismatch between our waveform model and hybrid waveforms in Table VII. For all the cases, the value of mismatch is smaller than $\approx 2 \times 10^{-5}$. According to our previous results [42], these values indicate that the the signal to noise ratio of the

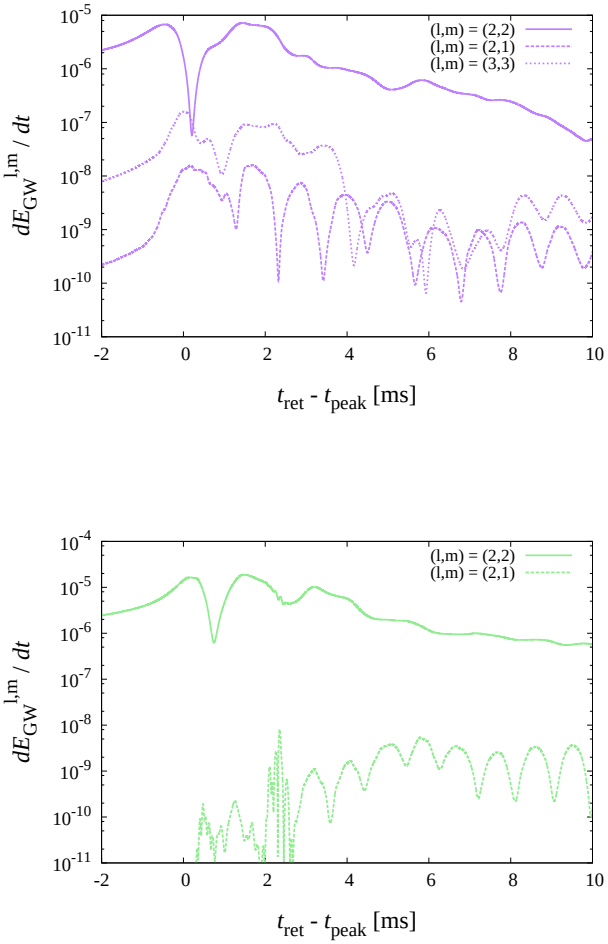

FIG. 21. (Top) Gravitational-wave energy flux (2.10) for $(l, m) = (2, 2)$, $(2, 1)$, and $(3, 3)$ modes for 15H107-146 with $N = 182$. (Bottom) The same as the top panel, but for $(l, m) = (2, 2)$ and $(2, 1)$ modes for 125H125-125 with $N = 182$.

difference between our waveform model and hybrid waveforms becomes as large as 1 only when the total signal to noise ratio is as large as 200.

V. SUMMARY

We performed long-term inspiral simulations for new 26 models of the non-spinning BNSs in numerical relativity. To derive high-precision gravitational waveforms in a large parameter space, we systematically vary the EOSs of NS, the chirp mass, and the mass ratio. To assess gravitational-wave phase error stemming from a finite grid resolution, we change the grid spacing by a factor of two in each binary model.

First, we found that the residual gravitational-wave phase error at the peak time of gravitational waves is $\lesssim 0.5$ radian irrespective of the binary models. By comparing the results for the piece-wise polytropic EOS and SFHo (tabulated) EOS models, we also found that the interpolation of the thermodynamic quantities during the simulations generates the phase error of $\approx$ 0.2–0.3 radian. However the gravitational-wave phase error for the SFHo (tabulated) EOS model still remains within the sub-radian level.

Second, we assessed the universal relations between the gravitational wave related quantities and the binary tidal deformability/NS radius proposed in the literature [54–60]. We found that the gravitational-wave frequency at the peak time $f_{\rm peak}$, the gravitational-wave amplitude at the peak time $h_{\rm peak}$, and the peak frequency f_2 associated with the f–mode oscillation of the remnant massive NS in the power spectrum density of gravitational waves depend strongly on the symmetric mass ratio and/or the grid resolution. This clearly illustrates that the universal relations proposed in the literature [54–60] are not very universal.

We proposed improved fitting formulae (3.3), (3.4),

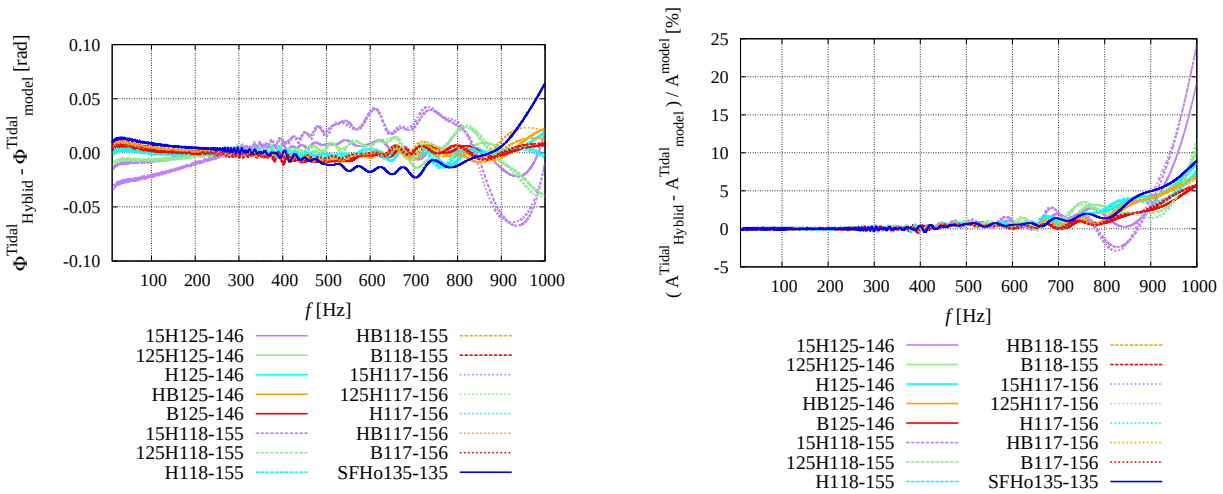

FIG. 22. (Left) Difference in the tidal-part phase between the hybrid waveforms and the model given by Eq. (4.6) for the binaries with $\mathcal{M}_c = 1.1752 M_\odot$. Phase differences are plotted after the alignment in the frequency range of 10–1000, Hz. (Right) Relative difference of tidal-part amplitude between the hybrid waveforms and the model given by Eq. (4.7).

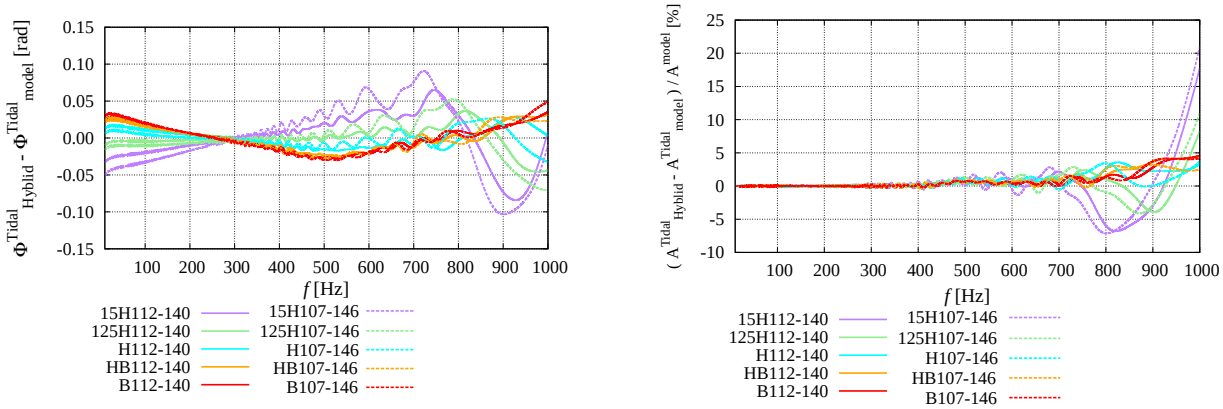

FIG. 23. The same as in Fig. 22 but for the models with $\mathcal{M}_c = 1.0882\, M_\odot$.

and (3.6). Note that these fitting formulae may still suffer from systematics as well because NS spin, NS magnetic fields, or the neutrino radiation is not taken into account in our simulations. We also found that f_1 frequency in the power spectrum density could be visible only for the nearly symmetric binaries. Unless we can determine the symmetric mass ratio accurately by gravitational wave data analysis, the universal relation for f_1 could derive a misleading result.

Third, we assessed the energy, $E_{\rm GW}$, and angular momentum, $J_{\rm GW}$, carried by gravitational waves in the inspiral and post-merger stages. As proposed in Ref. [56], the correlation between $E^{\rm tot}_{\rm GW,i}$ and the binary tidal deformability is tight and does not depend significantly on the symmetric mass ratio. We found that the relation $E_{\rm GW} \approx \pi f_2 J_{\rm GW}$ is nicely satisfied in the post-merger gravitational wave signal irrespective of the binary models because the signal from the remnant NSs is approximately monochromatically emitted by the f–mode oscillation. The angular momentum of the remnant massive NS, $J_{\rm rem}$, correlates with the binary tidal deformability. This quantity is relevant to build a model of post-merger evolution of merger remnants [91].

Finally, we validated our SACRA gravitational waveform template [42] with the high-precision gravitational waveforms derived in this paper. We found that for a variety of BNS models the systematics associated with the waveform modeling is less than 0.1 radian in the gravitational-wave phase and less than 20% in the amplitude up to $f_{\rm GW} = 1000$ Hz. This SACRA gravitational waveform template can be used for a new gravitational wave data analysis for extracting tidal deformability from GW170817 and for a future event of BNS merger. Our waveform data are publicly available on the web page.

ACKNOWLEDGMENTS

Numerical computations were performed on K computer at AICS (project numbers hp160211, hp170230, hp170313, hp180179, hp190160), on Cray XC50 at cfca of National Astronomical Observatory of Japan, Oakforest-PACS at Information Technology Center of the University of Tokyo, and on Cray XC30 at Yukawa Institute for Theoretical Physics, Kyoto University. This work was supported by Grant-in-Aid for Scientific Research (16H02183, 16H06342, 16H06341, 16K17706, 17H01131, 17H06361, 17H06363, 18H01213, 18H04595, 18H05236, 18K03642, 19H14720) of JSPS and by a post-K computer project (Priority issue No. 9) of Japanese MEXT.

[1] B. P. Abbott *et al.* [LIGO Scientific and Virgo Collaborations], Phys. Rev. Lett. **119**, no. 16, 161101 (2017)
[2] B. P. Abbott *et al.* [LIGO Scientific and Virgo and Fermi-GBM and INTEGRAL Collaborations], Astrophys. J. **848**, no. 2, L13 (2017)
[3] A. Goldstein *et al.*, Astrophys. J. **848**, no. 2, L14 (2017)
[4] V. Savchenko *et al.*, Astrophys. J. **848**, no. 2, L15 (2017)
[5] P. A. Evans *et al.*, Science **358**, 1565 (2017)
[6] M. R. Drout *et al.*, Science **358**, 1570 (2017)
[7] C. D. Kilpatrick *et al.*, Science **358**, no. 6370, 1583 (2017)
[8] M. M. Kasliwal *et al.*, Science **358**, 1559 (2017)
[9] M. Nicholl *et al.*, Astrophys. J. **848**, no. 2, L18 (2017)
[10] Y. Utsumi *et al.* [J-GEM Collaboration], Publ. Astron. Soc. Japan **69**, 101 (2017)
[11] N. Tominaga *et al.*, Publ. Astron. Soc. Japan **70**, 28 (2018)
[12] R. Chornock *et al.*, Astrophys. J. **848**, no. 2, L19 (2017)
[13] I. Arcavi *et al.*, Astrophys. J. **848**, no. 2, L33 (2017)
[14] M. C. Diaz *et al.* [TOROS Collaboration], Astrophys. J. **848**, no. 2, L29 (2017)
[15] B. J. Shappee *et al.*, Science **358**, 1574 (2017)
[16] D. A. Coulter *et al.*, Science **358**, 1556 (2017)
[17] M. Soares-Santos *et al.* [DES and Dark Energy Camera GW-EM Collaborations], Astrophys. J. **848**, no. 2, L16 (2017)
[18] S. Valenti *et al.*, Astrophys. J. **848**, no. 2, L24 (2017)
[19] E. Pian *et al.*, Nature **551**, 67 (2017)
[20] S. J. Smartt *et al.*, Nature **551**, no. 7678, 75 (2017)
[21] D. Haggard, M. Nynka, J. J. Ruan, V. Kalogera, S. Bradley Cenko, P. Evans and J. A. Kennea, Astrophys. J. **848**, no. 2, L25 (2017)
[22] R. Margutti *et al.*, Astrophys. J. **848**, no. 2, L20 (2017)
[23] E. Troja *et al.*, Nature **551**, 71 (2017)
[24] K. D. Alexander *et al.*, Astrophys. J. **848**, no. 2, L21 (2017)
[25] G. Hallinan *et al.*, Science **358**, 1579 (2017)
[26] R. Margutti *et al.*, Astrophys. J. **856**, no. 1, L18 (2018)
[27] D. Dobie *et al.*, arXiv:1803.06853 [astro-ph.HE].
[28] K. P. Mooley *et al.*, Nature **554**, 207 (2018)
[29] K. P. Mooley *et al.*, Nature **561**, no. 7723, 355 (2018)
[30] LIGO & Collaborations, V., GRB Coordinates Network, Circular Service, No 24237 (2019): LIGO & Collaborations, V., GRB Coordinates Network, Circular Service, No 24228 (2019): LIGO & Collaborations, V., GRB Coordinates Network, Circular Service, No 24168 (2019)
[31] E. E. Flanagan and T. Hinderer, Phys. Rev. D **77**, 021502 (2008)
[32] B. P. Abbott *et al.* [LIGO Scientific and Virgo Collaborations], Phys. Rev. Lett. **121**, no. 16, 161101 (2018)
[33] S. De, D. Finstad, J. M. Lattimer, D. A. Brown, E. Berger and C. M. Biwer, Phys. Rev. Lett. **121**, no. 9, 091102 (2018) Erratum: [Phys. Rev. Lett. **121**, no. 25, 259902 (2018)]
[34] B. P. Abbott *et al.* [LIGO Scientific and Virgo Collaborations], Phys. Rev. X **9**, no. 1, 011001 (2019)
[35] T. Dietrich, N. Moldenhauer, N. K. Johnson-McDaniel, S. Bernuzzi, C. M. Markakis, B. Brgmann and W. Tichy, Phys. Rev. D **92**, no. 12, 124007 (2015)
[36] T. Dietrich and T. Hinderer, Phys. Rev. D **95**, no. 12, 124006 (2017)
[37] T. Dietrich, S. Bernuzzi and W. Tichy, Phys. Rev. D **96**, no. 12, 121501 (2017)
[38] T. Dietrich *et al.*, Phys. Rev. D **99**, no. 2, 024029 (2019)
[39] T. Dietrich *et al.*, Class. Quant. Grav. **35**, no. 24, 24LT01 (2018)
[40] T. Dietrich, A. Samajdar, S. Khan, N. K. Johnson-McDaniel, R. Dudi and W. Tichy, arXiv:1905.06011 [gr-qc].
[41] K. Kiuchi, K. Kawaguchi, K. Kyutoku, Y. Sekiguchi, M. Shibata and K. Taniguchi, Phys. Rev. D **96**, no. 8, 084060 (2017)
[42] K. Kawaguchi, K. Kiuchi, K. Kyutoku, Y. Sekiguchi, M. Shibata and K. Taniguchi, Phys. Rev. D **97**, no. 4, 044044 (2018)
[43] R. Haas *et al.*, Phys. Rev. D **93**, no. 12, 124062 (2016)
[44] F. Foucart *et al.*, Phys. Rev. D **99**, no. 4, 044008 (2019)
[45] M. Shibata, Phys. Rev. Lett. **94**, 201101 (2005)
[46] K. Hotokezaka, K. Kyutoku and M. Shibata, Phys. Rev. D **87**, no. 4, 044001 (2013)
[47] K. Hotokezaka, K. Kyutoku, H. Okawa and M. Shibata, Phys. Rev. D **91**, no. 6, 064060 (2015)
[48] K. Hotokezaka, K. Kyutoku, Y. i. Sekiguchi and M. Shibata, Phys. Rev. D **93**, no. 6, 064082 (2016)
[49] T. Damour, A. Nagar, and L. Villain Phys. Rev. D **85**, 123007 (2012)
[50] J. Vines, E. E. Flanagan and T. Hinderer, Phys. Rev. D **83**, 084051 (2011)
[51] B. P. Abbott *et al.* [LIGO Scientific and Virgo Collaborations], Astrophys. J. **851**, no. 1, L16 (2017)
[52] M. Punturo *et al.*, Class. Quant. Grav. **27**, 194002 (2010).
[53] B. P. Abbott *et al.* [LIGO Scientific Collaboration], Class. Quant. Grav. **34**, no. 4, 044001 (2017)
[54] J. S. Read *et al.*, Phys. Rev. D **88**, 044042 (2013) doi:10.1103/PhysRevD.88.044042
[55] L. Rezzolla and K. Takami, Phys. Rev. D **93**, no. 12, 124051 (2016)
[56] F. Zappa, S. Bernuzzi, D. Radice, A. Perego and T. Dietrich, Phys. Rev. Lett. **120**, no. 11, 111101 (2018)
[57] S. Bernuzzi, A. Nagar, T. Dietrich and T. Damour, Phys. Rev. Lett. **114**, no. 16, 161103 (2015)
[58] S. Bernuzzi, T. Dietrich and A. Nagar, Phys. Rev. Lett. **115**, no. 9, 091101 (2015)

[59] A. Bauswein, H. T. Janka, K. Hebeler and A. Schwenk, Phys. Rev. D **86**, 063001 (2012)
[60] A. Bauswein and H.-T. Janka, Phys. Rev. Lett. **108**, 011101 (2012)
[61] T. Yamamoto, M. Shibata and K. Taniguchi, Phys. Rev. D **78**, 064054 (2008)
[62] M. Shibata and T. Nakamura, Phys. Rev. D **52**, 5428, (1995).
[63] T. W. Baumgarte and S. L. Shapiro, Phys. Rev. D **59**, 024007 (1998).
[64] M. Campanelli, C. O. Lousto, P. Marronetti, and Y. Zlochower, Phys. Rev. Lett. **96**, 111101 (2006).
[65] J. G. Baker, J. Centrella, D.-I. Choi, M. Koppitz, and J. van Meter, Phys. Rev. Lett. **96**, 111102 (2006).
[66] D. Hilditch, S. Bernuzzi, M. Thierfelder, Z. Cao, W. Tichy and B. Bruegmann, Phys. Rev. D **88**, 084057 (2013)
[67] B. Bruegmann, J. A. Gonzalez, M. Hannam, S. Husa, U. Sperhake and W. Tichy, Phys. Rev. D **77**, 024027 (2008)
[68] A. Kurganov and E. Tadmor, J. Comput. Phys. **160**, 241 (2000).
[69] P. Colella and P. R. Woodward, J. Comput. Phys. **54**, 174 (1984).
[70] M. J. Berger and J. Oliger, J. Comput. Phys. **53**, 484 (1984)
[71] J. S. Read, B. D. Lackey, B. J. Owen, and J. L. Friedman, Phys. Rev. D **79**, 124032 (2009).
[72] A. W. Steiner, M. Hempel and T. Fischer, Astrophys. J. **774**, 17 (2013)
[73] LORENE webpage:http://www.lorene.obspm.fr/
[74] K. Taniguchi and M. Shibata, Astrophys. J. **188**, 187 (2010): K. Taniguchi and E. Gourgoulhon, Phys. Rev. D **68**, 124025 (2003): K. Taniguchi and E. Gourgoulhon, Phys. Rev. D **66**, 104019 (2002)
[75] K. Kyutoku, M. Shibata and K. Taniguchi, Phys. Rev. D **90**, no. 6, 064006 (2014)
[76] H. Nakano, Class. Quantum. Grav. **32**, 177002 (2015)
[77] C. Reisswig and D. Pollney, Class. Quant. Grav. **28**, 195015 (2011)
[78] M. Shibata, "Numerical Relativity (100 years of General Relativity)" (2015), World Scientific Publishing Co Pte Ltd (20 May 2002)
[79] https://www2.yukawa.kyoto-u.ac.jp/~nr_kyoto/SACRA_PUB/catalog.html
[80] K. Hotokezaka, K. Kiuchi, K. Kyutoku, T. Muranushi, Y. i. Sekiguchi, M. Shibata and K. Taniguchi, Phys. Rev. D **88**, 044026 (2013)
[81] L. Blanchet, Living Rev. Rel. **17**, 2 (2014)
[82] For the symmetric bianry, the tidal coupling constant κ_2^T is equal to $3\tilde{\Lambda}/16$.
[83] K. Kiuchi, K. Kyutoku, Y. Sekiguchi, M. Shibata and T. Wada, Phys. Rev. D **90**, 041502 (2014)
[84] K. Kiuchi, P. Cerdá-Durán, K. Kyutoku, Y. Sekiguchi and M. Shibata, Phys. Rev. D **92**, no. 12, 124034 (2015)
[85] T. Dietrich, S. Bernuzzi, M. Ujevic and B. Bruegmann, Phys. Rev. D **91**, no. 12, 124041 (2015)
[86] F. Foucart *et al.*, Phys. Rev. D **93**, no. 4, 044019 (2016)
[87] A. Bauswein and N. Stergioulas, Phys. Rev. D **91**, no. 12, 124056 (2015)
[88] M. Shibata, K. Taniguchi and K. Uryu, Phys. Rev. D **71**, 084021 (2005)
[89] The peak frequency in the power spectrum density is called as $f_{\rm peak}$ in Refs. [59, 60]. Because we define $f_{\rm peak}$ by the gravitational-wave frequency at the peak time of the gravitational-wave amplitude, we follow the convension in Ref. [55] to avoid confusion.
[90] S. Fujibayashi, K. Kiuchi, N. Nishimura, Y. Sekiguchi and M. Shibata, "Mass Ejection from the Remnant of Binary Neutron Star Merger: Viscous-Radiation Hydrodynamics Study," Astrophys. J. **860**, no. 1, 64 (2018)
[91] M. Shibata, E. Zhou, K. Kiuchi, and S. Fujibayashi, arxiv:1905.03656
[92] K. Kiuchi, K. Kyutoku, M. Shibata and K. Taniguchi, Astrophys. J. **876**, no. 2, L31 (2019)
[93] Y. Sekiguchi, K. Kiuchi, K. Kyutoku and M. Shibata, Phys. Rev. Lett. **107**, 051102 (2011)
[94] M. Shibata and K. Kiuchi, Phys. Rev. D **95**, no. 12, 123003 (2017)
[95] V. Paschalidis, W. E. East, F. Pretorius and S. L. Shapiro, Phys. Rev. D **92**, no. 12, 121502 (2015)
[96] D. Radice, S. Bernuzzi and C. D. Ott, Phys. Rev. D **94**, no. 6, 064011 (2016)
[97] J. Steinhoff *et al.*, Phys. Rev. D **94**, no. 10, 104028 (2016)
[98] T. Hinderer *et al.*, Phys. Rev. Lett. **116**, no. 18, 181101 (2016)
[99] B. Lackey *et al.*, arXiv:1812.08643 (2018)
[100] https://dcc.ligo.org/LIGO-T0900288/public

TABLE V. Binary tidal deformability $\tilde{\Lambda}$, $f_{\rm peak}$, $h_{\rm peak}$, f_2, $E^{2,2}_{\rm GW,i}$, $E^{2,2}_{\rm GW,p}$, $J^{2,2}_{\rm GW,p}$, $J_{\rm rem}$, and $m_0 - M_{\rm ADM,0}$. $M_{\rm ADM,0}$ is the Arnowitt-Deser-Misner mass of the initial condition of the simulations. We adopt 2% relative error for $f_{\rm peak}$ and $h_{\rm peak}$ and 5% relative error for f_2, respectively, as a typical value. For f_2, we exclude models which collapse to a black hole within a few ms after the merger. For $E^{2,2}_{\rm GW,i}$ and $J_{\rm rem}$, we adopt 2% and 1% relative error, respectively. $E_{\rm GW}$ and $m_0 - M_{\rm ADM,0}$ are given in the unit of $M_\odot c^2$. $J_{\rm GW}$ and $J_{\rm rem}$ are in the unit of $GM_\odot^2/c$.

Model	$\tilde{\Lambda}^{1/5}$	$f_{\rm peak}$ [Hz]	$Dh_{\rm peak}/m_0$	f_2[Hz]	$E^{2,2}_{{\rm GW},i}$	$E^{2,2}_{{\rm GW},p}$	$J^{2,2}_{{\rm GW},p}$	$J_{\rm rem}$	$m_0 - M_{\rm ADM,0}$
15H135-135	4.14	1503±30	0.226±0.005	2321±116	(7.90±0.16) × 10^{-3}	1.35×10^{-2}	0.40	6.64±0.07	1.65 × 10^{-2}
125H135-135	3.87	1652±33	0.236±0.005	2517±126	(9.04±0.18) × 10^{-3}	1.76×10^{-2}	0.48	6.54±0.07	1.64 × 10^{-2}
H135-135	3.60	1820±36	0.249±0.005	2790±139	(1.03±0.02) × 10^{-2}	2.32×10^{-2}	0.56	6.46±0.06	1.63 × 10^{-2}
HB135-135	3.35	1986±40	0.261±0.005	3243±162	(1.17±0.02) × 10^{-2}	2.89×10^{-2}	0.59	6.39±0.06	1.64 × 10^{-2}
B135-135	3.11	2133±43	0.274±0.005	–	(1.30±0.03) × 10^{-2}	7.39×10^{-3}	0.13	6.33±0.06	1.65 × 10^{-2}
15H121-151	4.13	1356±27	0.212±0.004	2261±163	(7.47±0.15) × 10^{-3}	5.47×10^{-3}	0.17	6.66±0.07	1.66 × 10^{-2}
125H121-151	3.86	1490±30	0.224±0.004	2379±119	(8.53±0.17) × 10^{-3}	8.24×10^{-3}	0.23	6.57±0.07	1.66 × 10^{-2}
H121-151	3.60	1637±33	0.236±0.005	2749±137	(9.70±0.19) × 10^{-3}	1.05×10^{-2}	0.26	6.49±0.06	1.66 × 10^{-2}
HB121-151	3.35	1809±36	0.249±0.005	3268±161	(1.10±0.02) × 10^{-2}	2.26×10^{-2}	0.48	6.41±0.06	1.66 × 10^{-2}
B121-151	3.11	1994±40	0.263±0.005	–	(1.23±0.02) × 10^{-2}	6.85×10^{-3}	0.13	6.35±0.06	1.66 × 10^{-2}
15H125-125	4.51	1450±29	0.211±0.004	2159±108	(6.26±0.13) × 10^{-3}	7.98×10^{-3}	0.25	5.95±0.06	1.53 × 10^{-2}
125H125-125	4.23	1568±31	0.222±0.004	2350±118	(7.19±0.14) × 10^{-3}	9.29×10^{-3}	0.27	5.87±0.06	1.53 × 10^{-2}
H125-125	3.95	1710±34	0.234±0.005	2749±137	(8.15±0.16) × 10^{-3}	1.67×10^{-2}	0.42	5.80±0.06	1.52 × 10^{-2}
HB125-125	3.69	1900±38	0.245±0.005	2873±144	(9.35±0.19) × 10^{-3}	1.66×10^{-2}	0.39	5.74±0.06	1.53 × 10^{-2}
B125-125	3.43	2099±42	0.257±0.005	3353±168	(1.06±0.02)) × 10^{-2}	2.19×10^{-2}	0.44	5.69±0.06	1.53 × 10^{-2}
15H116-158	4.12	1273±26	0.205±0.004	2148±107	(7.19±0.14) × 10^{-3}	4.63×10^{-3}	0.15	6.84±0.07	1.65 × 10^{-2}
125H116-158	3.85	1406±28	0.214±0.004	2276±124	(8.20±0.16) × 10^{-3}	1.01×10^{-2}	0.28	6.76±0.07	1.65 × 10^{-2}
H116-158	3.60	1540±31	0.227±0.005	2767±138	(9.30±0.19) × 10^{-3}	1.23×10^{-2}	0.31	6.69±0.07	1.66 × 10^{-2}
HB116-158	3.35	1709±34	0.240±0.005	3242±162	(1.05±0.02) × 10^{-2}	1.40×10^{-2}	0.30	6.63±0.06	1.65 × 10^{-2}
B116-158	3.11	1885±37	0.254±0.005	–	(1.18±0.02) × 10^{-2}	4.64×10^{-3}	0.10	6.58±0.07	1.65 × 10^{-2}
15H125-146	4.13	1401±28	0.214±0.004	2336±117	(7.62±0.02) × 10^{-3}	1.01×10^{-2}	0.30	6.81±0.07	1.66 × 10^{-2}
125H125-146	3.86	1560±31	0.226±0.005	2576±129	(8.77±0.18) × 10^{-3}	1.26×10^{-2}	0.34	6.73±0.07	1.66 × 10^{-2}
H125-146	3.60	1691±34	0.238±0.003	2827±141	(9.91±0.20) × 10^{-3}	1.89×10^{-2}	0.45	6.66±0.07	1.66 × 10^{-2}
HB125-146	3.35	1856±37	0.252±0.005	3251±163	(1.12±0.20) × 10^{-2}	2.50×10^{-2}	0.52	6.60±0.07	1.66 × 10^{-2}
B125-146	3.11	2039±41	0.265±0.005	–	(1.26±0.25) × 10^{-2}	7.99×10^{-3}	0.14	6.56±0.06	1.66 × 10^{-2}
15H118-155	4.12	1308±26	0.206±0.004	2161±108	(7.31±0.15) × 10^{-3}	5.72×10^{-3}	0.18	6.83±0.07	1.66 × 10^{-2}
125H118-155	3.86	1441±29	0.218±0.004	2358±118	(8.35±0.17) × 10^{-3}	7.12×10^{-3}	0.21	6.75±0.07	1.67 × 10^{-2}
H118-155	3.60	1590±32	0.230±0.005	2782±139	(9.49±0.19) × 10^{-3}	1.59×10^{-2}	0.39	6.68±0.07	1.66 × 10^{-2}
HB118-155	3.35	1759±35	0.243±0.005	3259±163	(1.08±0.02) × 10^{-2}	2.03×10^{-2}	0.43	6.62±0.07	1.66 × 10^{-2}
B118-155	3.11	1942±39	0.257±0.005	–	(1.20±0.02) × 10^{-2}	5.54×10^{-3}	0.11	6.66±0.07	1.66 × 10^{-2}
15H117-156	4.11	1293±26	0.204±0.004	2161±108	(7.26±0.15) × 10^{-3}	5.09×10^{-3}	0.17	6.83±0.07	1.66 × 10^{-2}
125H117-156	3.84	1425±29	0.216±0.004	2416±121	(8.30±0.17) × 10^{-3}	8.09×10^{-3}	0.23	6.76±0.07	1.66 × 10^{-2}
H117-156	3.58	1574±32	0.229±0.005	2775±139	(9.43±0.19) × 10^{-3}	1.39×10^{-2}	0.34	6.69±0.07	1.66 × 10^{-2}
HB117-156	3.34	1724±35	0.242±0.005	3201±160	(1.06±0.02) × 10^{-2}	1.61×10^{-2}	0.35	6.62±0.07	1.66 × 10^{-2}
B117-156	3.10	1933±38	0.256±0.005	–	(1.20±0.02) × 10^{-2}	5.26×10^{-3}	0.11	6.58±0.06	1.64 × 10^{-2}
15H112-140	4.50	1281±26	0.197±0.004	2188±109	(5.91±0.12) × 10^{-3}	5.37×10^{-3}	0.17	5.97±0.06	1.49 × 10^{-2}
125H112-140	4.21	1412±28	0.208±0.004	2269±113	(6.80±0.14) × 10^{-3}	4.80×10^{-3}	0.15	5.89±0.06	1.49 × 10^{-2}
H112-140	3.94	1558±31	0.220±0.004	2470±123	(7.78±0.16) × 10^{-3}	6.18×10^{-3}	0.17	5.82±0.06	1.50 × 10^{-2}
HB112-140	3.68	1717±34	0.231±0.005	2791±140	(8.84±0.18) × 10^{-3}	9.52×10^{-3}	0.23	5.76±0.06	1.50 × 10^{-2}
B112-140	3.43	1890±38	0.244±0.005	3271±164	(9.98±0.20) × 10^{-3}	1.59×10^{-2}	0.33	5.71±0.06	1.52 × 10^{-2}
15H107-146	4.50	1203±24	0.189±0.004	2054±103	(5.70±0.11) × 10^{-3}	3.63×10^{-3}	0.13	5.99±0.06	1.51 × 10^{-2}
125H107-146	4.22	1328±27	0.200±0.004	2291±115	(6.57±0.13) × 10^{-3}	4.56×10^{-3}	0.14	5.91±0.06	1.50 × 10^{-2}
H107-146	3.94	1475±30	0.212±0.004	2546±127	(7.49±0.15) × 10^{-3}	7.82×10^{-3}	0.21	5.84±0.06	1.49 × 10^{-2}
HB107-146	3.69	1620±32	0.224±0.004	2870±143	(8.51±0.17) × 10^{-3}	1.02×10^{-2}	0.25	5.78±0.06	1.50 × 10^{-2}
B107-146	3.44	1786±36	0.237±0.005	3298±165	(9.60±0.19) × 10^{-3}	1.29×10^{-2}	0.27	5.73±0.06	1.51 × 10^{-2}
SFHo135-135	3.41	1987±40	0.261±0.005	3250±163	(1.17±0.02) × 10^{-2}	2.91×10^{-3}	0.61	6.60±0.07	1.68 × 10^{-2}

TABLE VI. Summary of the assessment of the universal relations for the non-spinning and non-magnetized binaries. Neutrino radiation is not taken into account. We show the maximum relative errors produced by the original relation (upper row) and by the improved relation in this paper (lower row). For f_1, the error is unable to be estimated because of the absence of f_1 peak in the asymmetric binaries. Therefore, we conclude there is no universal relation between f_1 and $\tilde{\Lambda}$. For $E^{2,2}_{\rm GW,p}$ and $J^{2,2}_{\rm GW,p}$, the error is unable to be estimated because uncertainties of the life time of the merger remnant NSs are large. For $R_{1.6}$–$\tilde{\Lambda}^{1/5}$ relation, we do not propose an improved relation.

$f_{\rm peak}$–$\tilde{\Lambda}^{1/5}$	$h_{\rm peak}$–$\tilde{\Lambda}^{1/5}$	f_1–$\tilde{\Lambda}^{1/5}$	f_2–$\tilde{\Lambda}^{1/5}$	f_2–$R_{1.6}$	$E^{2,2}_{\rm GW,i}$–$\tilde{\Lambda}^{1/5}$	$E^{2,2}_{\rm GW,p}$–$\tilde{\Lambda}^{1/5}$	$J^{2,2}_{\rm GW,p}$–$\tilde{\Lambda}^{1/5}$	$J_{\rm rem}$–$\tilde{\Lambda}^{1/5}$
$\approx 17\%$	N/A	–	$\approx 14\%$	$\approx 10\%$	N/A	N/A	N/A	N/A
$\approx 3\%$	$\approx 4\%$	–	$\approx 9\%$	–	$\approx 4\%$	–	–	$\approx 3\%$

TABLE VII. Mismatch between the waveform model and hybrid waveforms.

Model	$\bar{F}$ ($\times 10^{-5}$)
15H125-146	0.83
125H125-146	0.36
H125-146	0.29
HB125-146	0.28
B125-146	0.22
15H118-155	0.82
125H118-155	0.26
H118-155	0.30
HB118-155	0.32
B118-155	0.31
15H117-156	0.97
125H117-156	0.31
H117-156	0.25
HB117-156	0.30
B117-156	0.17
15H112-140	0.88
125H112-140	0.24
H112-140	0.37
HB112-140	0.71
B112-140	0.91
15H107-146	1.82
125H107-146	0.45
H107-146	0.30
HB107-146	0.79
B107-146	1.12
SFHo135-135	0.45